



UNIVERSITY OF LEEDS

This is a repository copy of *The characterisation of dental enamel using transmission Kikuchi diffraction in the scanning electron microscope combined with dynamic template matching*.

White Rose Research Online URL for this paper:

<https://eprints.whiterose.ac.uk/209323/>

Version: Accepted Version

Article:

Trimby, P., Al-Mosawi, M., Al-Jawad, M. et al. (4 more authors) (Cover date: June 2024)

The characterisation of dental enamel using transmission Kikuchi diffraction in the scanning electron microscope combined with dynamic template matching.

Ultramicroscopy, 260. 113940. ISSN 0304-3991

<https://doi.org/10.1016/j.ultramic.2024.113940>

© 2024, Elsevier. This manuscript version is made available under the CC-BY-NC-ND 4.0 license <http://creativecommons.org/licenses/by-nc-nd/4.0/>.

Reuse

This article is distributed under the terms of the Creative Commons Attribution-NonCommercial-NoDerivs (CC BY-NC-ND) licence. This licence only allows you to download this work and share it with others as long as you credit the authors, but you can't change the article in any way or use it commercially. More information and the full terms of the licence here: <https://creativecommons.org/licenses/>

Takedown

If you consider content in White Rose Research Online to be in breach of UK law, please notify us by emailing eprints@whiterose.ac.uk including the URL of the record and the reason for the withdrawal request.



eprints@whiterose.ac.uk
<https://eprints.whiterose.ac.uk/>

1 **The characterisation of dental enamel using transmission Kikuchi diffraction in the scanning**
2 **electron microscope combined with dynamic template matching**

3

4 Patrick Trimby^{1,6}, Mohammed Al-Mosawi², Maisoon Al-Jawad², Stuart Micklethwaite³, Zabeada
5 Aslam³, Aimo Winkelmann⁴ and Sandra Piazzolo⁵

6 1. Oxford Instruments Nanoanalysis, High Wycombe, Buckinghamshire, UK

7 2. School of Dentistry, University of Leeds, Leeds, West Yorkshire, UK

8 3. School of Chemical and Process Engineering, University of Leeds, Leeds, West Yorkshire, UK

9 4. ST Development GmbH, Paderborn, Germany

10 5. School of Earth and Environment, University of Leeds, Leeds, West Yorkshire, UK

11 6. Carl Zeiss Ltd., Cambourne, Cambridge, UK

12

13 **Abstract**

14 The remarkable physical properties of dental enamel can be largely attributed to the structure of the
15 hydroxyapatite (HAp) crystallites on the sub-micrometre scale. Characterising the HAp
16 microstructure is challenging, due to the nanoscale of individual crystallites and practical challenges
17 associated with HAp examination using electron microscopy techniques. Conventional methods for
18 enamel characterisation include imaging using transmission electron microscopy (TEM) or
19 specialised beamline techniques, such as polarisation-dependent imaging contrast (PIC). These
20 provide useful information at the necessary spatial resolution but are not able to measure the full
21 crystallographic orientation of the HAp crystallites. Here we demonstrate the effectiveness of
22 enamel analyses using transmission Kikuchi diffraction (TKD) in the scanning electron microscope,
23 coupled with newly-developed pattern matching methods. The pattern matching approach, using
24 dynamic template matching coupled with subsequent orientation refinement, enables robust
25 indexing of even poor-quality TKD patterns, resulting in significantly improved data quality
26 compared to conventional diffraction pattern indexing methods. The potential of this method for the
27 analysis of nanocrystalline enamel structures is demonstrated by the characterisation of a human
28 enamel TEM sample and the subsequent comparison of the results to high resolution TEM imaging.
29 The TKD – pattern matching approach measures the full HAp crystallographic orientation enabling a
30 quantitative measurement of not just the c-axis orientations, but also the extent of any rotation of
31 the crystal lattice about the c-axis, between and within grains. Results presented here show how this
32 additional information highlights potentially significant aspects of the HAp crystallite structure,
33 including intra-crystallite distortion and the presence of multiple high angle boundaries between
34 adjacent crystallites with rotations about the c-axis. These and other observations enable a more
35 rigorous understanding of the relationship between HAp structures and the physical properties of
36 dental enamel.

37

38 **Keywords**

39 Enamel, Hydroxyapatite, Biomineralisation, Transmission Kikuchi Diffraction (TKD), Pattern
40 Matching, Dynamic Template Matching.

41

42 1. Introduction

43

44 Dental enamel is the outermost layer of the tooth that covers and protects the underlying dentine.
45 Unlike other mineralised tissues, dental enamel is acellular and hence lacks the ability to regenerate
46 or repair itself following traumatic events or pathological decay [1; Robinson et al., 2000]. Due to its
47 acellular composition, dental enamel emerges as the hardest and most mineralised tissue in the
48 human body [2; Robinson et al., 1995a] comprising of up to 98 wt. % mineral [3; Elliott, 1997]. The
49 mineral content had been identified as an impure, non-stoichiometric, calcium deficient, carbonated
50 hydroxyapatite (HAp) [3; Elliott, 1997] in the form of needle-like crystallites measuring
51 approximately 26 nm in thickness, 68 nm in width and up to several microns in lengths [4; Kerebel et
52 al., 1997]. These crystallites are tightly packed into bundles, known as prisms, in the order of 4-7 μm
53 in diameter extending from the enamel-dentine junction to the enamel surface [5-6; Simmer et al.,
54 2012; Shore et al., 1995a]. In human enamel, the cross sections of the majority of these prisms
55 resemble a keyhole shape with distinct head and tail regions [6-7; Shore et al., 1995a; Boyde, 1964].

56 The visualisation and assessment of intra-prismatic crystallite organisation and alignment are critical
57 to gain complete understanding of the properties and structure of dental enamel and the underlying
58 mechanisms of enamel biomineralisation and its relationship to dental health. This information can
59 assist in the identification of potential causes of enamel defects and disorders and provide insight
60 into the tooth response to the various types of forces and stresses it is subjected to during biting and
61 mastication [8; Lawn et al., 2010].

62 Early studies examining the arrangement of crystallites within prisms in enamel have primarily
63 utilised electron microscopy techniques. It has been observed that the c-axes of the crystallites at
64 the head are predominately oriented parallel to the long axis of the prism, with minor variations.
65 However, the crystallites in the tail region are angled at approximately 45-70° to the direction of the
66 prism long axis [6, 9-11; Shore et al., 1995a, 1995b; Robinson et al., 1995b; Poole and Brooks, 1961].

67 Recent advances in imaging techniques have provided new insights into the organisation,
68 orientation, and properties of intra-prismatic crystallites. Recent studies using polarisation-
69 dependent imaging contrast (PIC) mapping to assess human enamel with a pixel size range of 22-
70 57 nm along the normal of the sample surface suggested that the long axis of each crystallite is not
71 always co-aligned in the head region; they can be as much as 90° apart [12; Beniash et al., 2019]. It
72 was concluded that the observed mis-orientation is most likely a crack-deflecting and toughening
73 mechanism against the high loading forces resulting from biting and mastication [12-13; Beniash et
74 al., 2019; Stifler et al., 2021]. It is important to note that the PIC mapping technique can only assess
75 the enamel surface to a depth of 3 nm, with 1 nm of this being a Pt coating and it only provides the
76 c-axis crystal orientations of HAp and not the full crystal orientation. Given that the typical
77 dimensions of HAp crystallites in enamel are significantly larger [4; Kerebel et al., 1979], it is
78 questionable whether the technique is capable of providing accurate data on enamel structure. Free
79 et al. used a combination of synchrotron X-ray diffraction, crystallite orientation analyses, and
80 machine learning to investigate the intra-prismatic variations in crystallographic parameters in
81 enamel. Their study revealed distinct compositions among inter-prismatic crystallites. It is worth
82 noting that the step size of 500 nm utilised, while capable of identifying intra-prismatic features, is
83 still markedly larger than the typical size of an individual crystallite [14-15; Free et al., 2020; 2022].

84 One technique that does provide full crystallographic orientations with a sub-100 nm spatial
85 resolution is electron backscatter diffraction (EBSD). EBSD is a scanning electron microscope (SEM)

86 based technique that is used extensively for the characterisation of crystalline microstructures,
87 including metals, alloys, ceramics and minerals [e.g. 16-17; Zaefferer, 2011; Borrajo-Pelaez and
88 Hedström, 2017]. The spatial resolution of EBSD is typically quoted as being in the order of 50-100
89 nm, but this is often a measure of the “effective” spatial resolution, influenced by the analysis
90 software’s ability to deconvolve overlapping diffraction patterns from neighbouring crystallites. The
91 true spatial resolution of the technique can be significantly poorer, especially at higher beam
92 energies or for the analysis of low atomic number materials. For example, for Mg, previous work has
93 indicated a true EBSD spatial resolution of ~600 nm at 15 keV beam energy, with an even worse
94 resolution down the steeply tilted surface that is required for conventional EBSD [18; Tripathi &
95 Zaefferer, 2019]. Given that HAp has a comparable atomic number to Mg, it is reasonable to expect
96 a similar spatial resolution for the EBSD analysis of HAp microstructures. There have been a number
97 of studies showing the potential of EBSD to characterise apatite-based microstructures, such as for
98 the study of conodont fossil structures (e.g. 19-20; Pérez-Huerta et al., 2012, Atakul-Özdemir et al.
99 2021) or in studies of shocked microstructures (e.g. 21; McGregor et al., 2021). However, these all
100 involve microstructures on the scale of 10s to 100s μm , for which the spatial resolution of EBSD is
101 sufficient and the effect of electron beam damage can be minimised.

102 However, the sub- μm size and distorted nature of HAp crystallites in tooth enamel make EBSD
103 analyses exceptionally challenging, as the source volume for each diffraction pattern is likely to
104 include orientations from multiple adjacent crystallites, thus significantly reducing the quality of any
105 resulting diffraction pattern. There has, therefore, been no reported successful EBSD analysis of
106 tooth enamel. A variation of EBSD, transmission Kikuchi diffraction (TKD), does hold much more
107 promise for the analysis of HAp structures in enamel. TKD, also sometimes referred to as
108 transmission EBSD (t-EBSD), involves the collection of Kikuchi diffraction patterns from an electron
109 transparent sample such as is typically prepared for imaging and analysis using the transmission
110 electron microscope (TEM). In TKD the diffraction pattern is projected from the lower (exit) surface
111 of the sample and this can be imaged either using a conventional EBSD detector with a (sub-) vertical
112 phosphor screen, or using a specially modified detector with a horizontal phosphor screen (“off-axis”
113 and “on-axis” TKD geometries, respectively) (22-25; Geiss and Keller, 2012; Trimby, 2012;
114 Funderberger et al., 2016; Sneddon et al., 2016). The major advantage of TKD over conventional
115 EBSD is the spatial resolution: with suitably thin samples, a lateral spatial resolution of sub 10 nm
116 has been demonstrated in various studies (e.g. 26; Shen et al., 2019), significantly better than is
117 possible with conventional EBSD. This makes TKD a potentially powerful technique for the analysis of
118 the nanostructured HAp crystallites in enamel, although the sensitivity of the material to damage
119 from the electron beam could limit the achievable spatial resolution in practice.

120 Two reported studies have already used TKD on enamel structures (27-28; Koblischka-Veneva et al.,
121 2018; 2019). These showed that the TKD method does enable the collection of indexable diffraction
122 patterns, however the results in both studies are questionable. For example, the diffraction pattern
123 and corresponding indexed solution shown in one study (Figure 7 d-e and Supplementary figure S1,
124 27; Koblischka-Veneva et al., 2018) clearly indicates incorrect indexing, with no correlation between
125 the observed and simulated Kikuchi bands. The subsequent orientation maps, despite a remarkable
126 5 nm step size, also show little correlation to the observed structures in corresponding TEM images
127 from the same samples, once again indicating poor or incorrect indexing possibly compounded by
128 over-aggressive data cleaning. This is further backed up by the blocky morphology of the crystallites
129 in the TKD orientation maps, with unusually straight boundaries between crystallites and no
130 evidence of the systematically elongated structures visible in the TEM images (e.g. Figures 2 and 3a,
131 28; Koblischka-Veneva et al., 2019). A lack of a reference image from the TKD-mapped area (such as

132 a diffraction pattern quality map or a bright- or dark field electron image) makes it difficult to have
133 any confidence in the veracity of these data.

134 In this work we revisit the use of TKD for the characterisation of tooth enamel nanostructures. As
135 demonstrated by Koblischka-Veneva and colleagues, TKD in the SEM does enable the collection of
136 indexable diffraction patterns. However, the pattern quality is highly variable and therefore newly-
137 developed pattern matching indexing and refinement methods may be necessary for effective
138 mapping of typical HAp microstructures. Such pattern matching methods use comparisons between
139 experimental diffraction patterns and simulated patterns that are generated using dynamical
140 modelling methods (e.g. 29-30; Winkelmann et al., 2007; Winkelmann, 2009). The first developed
141 pattern matching methods focused on dictionary indexing, in which a large precalculated library of
142 simulated patterns covering all possible crystallographic orientations would be compared to each
143 experimental pattern, with the best fitting template selected and the corresponding phase and
144 orientation saved (e.g. 31; Chen et al., 2015). This method was extremely time consuming and
145 resulted in a relatively low orientation precision, but it was demonstrated to give far better indexing
146 rates than conventional Hough-based indexing on samples that produced poor quality diffraction
147 patterns (e.g. 32; Singh et al., 2018). Other approaches have utilised a hybrid approach, in which
148 simulated diffraction patterns were calculated as required, based on the initial orientation from
149 Hough-based indexing (e.g. 33-35; Winkelmann et al., 2020; Winkelmann and Nolze, 2015; Nolze et
150 al., 2018). This approach enabled on-the-fly refinement of the orientation at each point, as well as
151 testing against pseudosymmetrically equivalent orientations, structure inversions or even against
152 phases with similar structures (e.g. 36; Nolze et al., 2017). Such pattern matching approaches have
153 developed in usability and speed since first being proposed and now offer a range of benefits
154 compared to conventional Hough-based indexing, both in terms of better indexing of poor quality
155 diffraction patterns as well as potentially a higher accuracy and precision in the final data.

156 Consequently, in this work we are exploring the further application of TKD, coupled with the latest
157 advances in pattern matching technology, to the study of dental enamel, which could assist in
158 elucidating new features of this complex, hierarchical structure. This research could have significant
159 implications for treating dental diseases and informing emerging biomimetic technologies that aim
160 to create materials that mimic the enamel microstructure.

161

162 **2. Material and Methods**

163

164 **2.1 Sample Selection and Preparation**

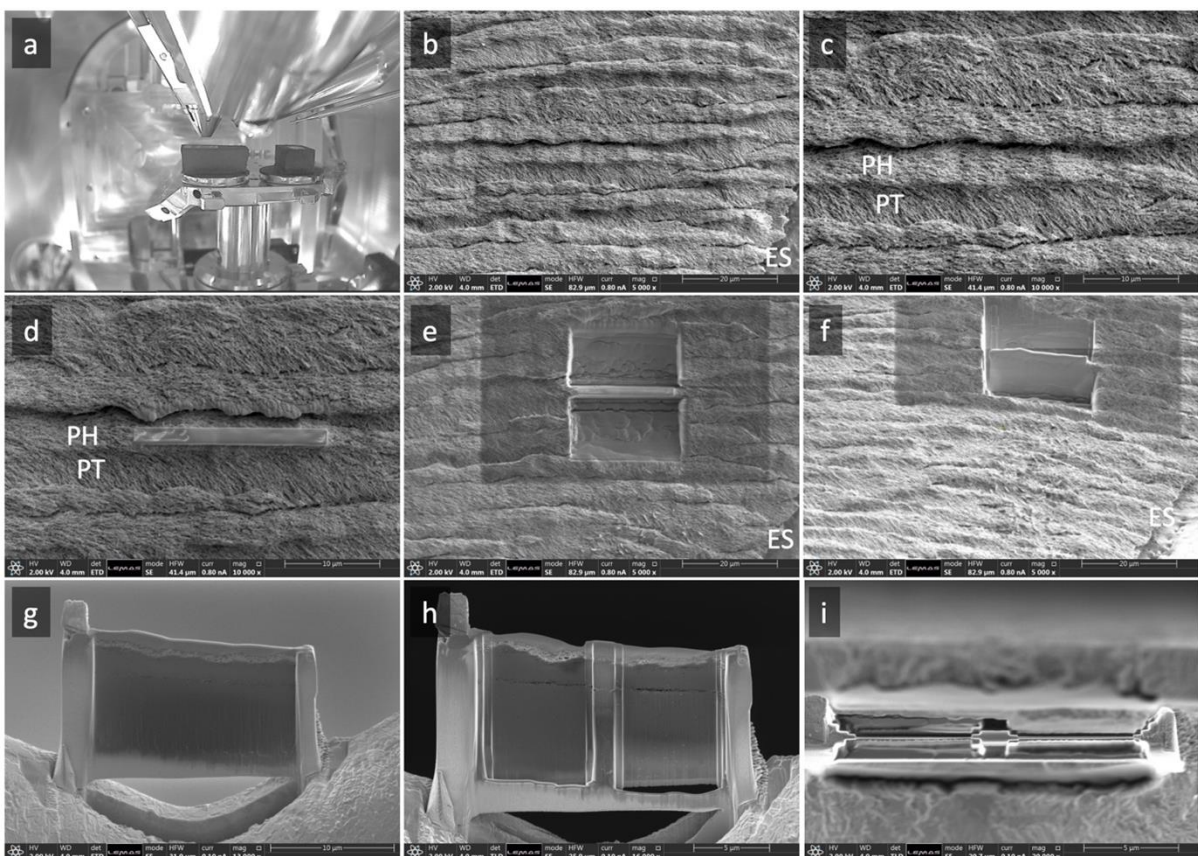
165 A healthy human premolar was obtained with ethical approval from the Leeds School of Dentistry
166 Tissue Bank (ref: 091219/MA/293). The tooth was embedded in fast curing acrylic cold mounting
167 resin (ClaroCit, Struers, Ballerup, Denmark) and cut mesio-distally through the mid-point into 2
168 halves using a Struers Accutom-10 diamond saw (Struers, Willich, Germany). The cut surface of the
169 buccal half of the tooth was then wet-ground using finer grades (100-, 220-, 320-, 400- and 600-grit)
170 of silicon carbide abrasive papers placing the tooth in distilled water between successive grits. The
171 cut surface was then etched using 20% orthophosphoric acid for 15 seconds.

172 The embedded section was washed with distilled water and secured onto an aluminium stub using
173 carbon adhesive disk. A 20 nm iridium coating was applied to eliminate contaminations [37; Xu et al.,
174 2022] and the resin and stub were carbon coated to avoid charging.

175 2.2. TEM Sample Preparation

176 For TEM imaging and TKD analysis, a thin sample lamella was prepared via the in-situ lift-out method
177 using a FEI Helios G4 CX dual beam, high resolution monochromated, field emission gun SEM with
178 precise focused ion beam (FIB-SEM).

179 Using the secondary electron detector, a region of interest (ROI) was identified and selected in a
180 manner that ensured it was contained within the prism head and aligned with its long axis (Figure 1).
181 In the FIB-SEM chamber, a 200 nm strip of platinum (Pt) was electron beam deposited (at 5 kV, 6.4
182 nA for the electron source) onto the ROI (100 × 20 μm) on the sample surface. This was followed by
183 a second Pt layer (2 μm) using ion assisted deposition of a Pt ion-rich precursor gas (at 30 kV, 0.23 nA
184 for the liquid gallium (Ga) ion source) at a 52° angle to the vertical electron beam. The Pt protective
185 layer dramatically decreases curtaining artefacts in the cross-sectioned enamel surface [38; Ishitani
186 et al., 2004] and protects the sample surface during milling [37; Xu et al., 2022]. The chamber
187 pressure was maintained to approximately 2×10^{-6} mbar (increases to 5×10^{-5} mbar during Pt
188 deposition). An initial lamella was cut (via FIB milling at 30 kV, 21 nA), before a final cut-out was
189 performed (at 30 kV, 0.79 nA). Final thinning and polishing of the lamellae to electron transparency
190 was performed with a low energy ion beam (5 kV, 41 pA). The lamella was then lifted using a
191 micromanipulator and welded using ion beam deposited Pt onto a copper FIB lift-out grid
192 (Omniprobe, Oxford Instruments, UK). The thickness of the lamella was measured using high
193 resolution electron imaging in the FIB-SEM and varied between 70 and 100 nm.



194

195 **Figure 1.** Sample preparation for TEM and TKD using FIB milling and micromanipulation: (a) A
196 photograph of the sample in the FIB-SEM chamber. (b) SEM image showing the etched surface of the
197 enamel sample with visible prismatic structure. Scale bar 20 μm. (c) A magnified SEM image of (b).
198 Scale bar 10 μm. (d) The region of interest is shown coated with Pt. Scale bar 10 μm. (e, f) Milled out

199 *area around the ROI. Scale bars 20 μm . (g) Welded lamella to the tip of a grid prior to thinning. Scale*
200 *bar 10 μm . Final sample lamella after thinning to 70-100 nm viewed from (h) front and (i) top-down*
201 *perspective. Scale bars 5 μm . PH: Prism head. PT: Prism tail. ES: Enamel surface.*

202 2.3 SEM Imaging

203 The FIB-prepared sample was mounted onto an Omnipivot™ sample holder with a pre-tilt angle of
204 45° (backtilted). This was inserted into a Carl Zeiss Gemini 460 field emission gun SEM, with the
205 stage tilted to 45° so that the TEM sample was in a horizontal position. The sample chamber was
206 briefly cleaned using an integrated, chamber-mounted Evacron plasma cleaner (2 minutes at 20W
207 power) before the sample was positioned at a working distance of 8.6 mm.

208 The electron beam accelerating voltage was set to 30 kV, with a beam current of 3.9 nA, and the
209 EBSD detector (Symmetry S3 detector, Oxford Instruments) was positioned to the fully inserted
210 position. The lower foreshatter detectors (3 backscattered electron (BSE) diodes mounted below the
211 phosphor screen of the EBSD detector) were then used to generate dark field electron images (e.g.
212 Trimby et al., 2014) with 2046 x 1641 pixel resolution and a 60 μs dwell time for each pixel. The
213 scanning, image selection and subsequent TKD data collection were carried out using Oxford
214 Instruments' AZtec software, v6.0.

215 2.4 TKD Analysis

216 Following imaging, a suitable area in the thinnest part of the sample was selected for TKD analysis.
217 The EBSD detector was set to "Speed 1" mode (622 x 512 pixel resolution), using a low electronic
218 gain setting and a 100 ms exposure time for each diffraction pattern. A background image was
219 collected from the whole sample and was used, along with dynamic background correction, to
220 improve the quality and uniformity of the signal in the TKD patterns. An area of 3 x 4 μm was
221 analysed with a measurement step size of 20 nm and at an analysis rate of 9.3 measurements per
222 second (the total analysis time was just under 54 minutes). The TKD patterns were analysed using a
223 standard Hough-transform approach to detect the Kikuchi bands, using a full Hough resolution of
224 121 (60 in the AZtec software) and using the AZtec software's "Optimized Band Detection" mode.
225 The indexing was carried out with reference to a HAp structure (Space Group 176, P 6₃/m, unit cell a
226 = b = 9.4373 Å, c = 6.8881 Å) using 48 theoretically calculated reflectors. During the analysis the TKD
227 patterns at each measurement point were stored for further offline examination.

228 2.5 Reanalysis using Pattern Matching

229 The original TKD data, along with the stored TKD patterns, were exported into the Oxford
230 Instruments *.h5oina data format [39] which utilises the hierarchical data format 5 (HDF5) structure.
231 The data were loaded into the Oxford Instruments AZtecCrystal software (version 3.1) for further
232 processing using pattern matching methods, included as part of the "MapSweeper" functionality.

233 Firstly, a master simulation file for HAp was created, using the crystallographic information file (cif)
234 number 1526459 downloaded from the Crystallography Open Database [40] and based on the HAp
235 structure reported in [41; Ivanova et al., 2001]. Four additional HAp structures and compositions
236 (with trace amounts of Na and Mg), as described in Wilson et al. (1999) (labelled RGB, RQ1, RE1 and
237 RC1), were also used to create master simulations in order to test the influence of minor chemical
238 and structural variations; these had a negligible effect on the simulations and no discernible impact
239 on the pattern matching results (<1 % difference), so the initial HAp structure was used. The master
240 simulation file is a model of the electron diffraction intensities for all crystallographic orientations of
241 HAp, for a specific beam energy (here 30 kV). A full many-beam dynamical simulation method was

242 used, as described in Winkelmann (2009), with the following modelling parameters – minimum
243 intensity 20%, minimum lattice spacing 1.2 Å, Debye Waller factor 0.5 and a full resolution of 501 x
244 501 pixels. This master file typically takes approximately 5 minutes to create and is then valid for use
245 on all subsequent datasets for the specified phase, collected using the same beam energy.

246 During all stages of the pattern matching process, pattern templates (e.g. simulated TKD patterns)
247 for desired phases and crystallographic orientations are derived from the master simulation file,
248 using the local projection geometry for the analysis point in question, and are created at the desired
249 pixel resolution (either low resolution for initial indexing, or high resolution for calibration or for
250 orientation refinement). Each pattern template, as well as the experimental TKD pattern, was
251 weighted using a 2D Gaussian window function in order to give greater importance to the centres of
252 the patterns (where the experimental patterns have a higher signal to noise ratio) compared to the
253 noisier edges of the patterns. This weighting also minimises the impact of shadowing in the
254 experimental data, a common problem with off-axis TKD. The process is fully dynamic: templates are
255 not stored on disk but are, once generated, matched directly to the experimental diffraction pattern
256 to give a metric of image similarity and are then discarded. Here we use the normalised cross
257 correlation coefficient (R) to assess the quality of pattern matching (e.g. 42; Goshtasby, 2012). The
258 absolute value of R can range from 0 to 1, with a higher R value indicating a better match. As any 2
259 arbitrary images can be correlated and will give an absolute R value > 0, it is essential that a
260 minimum threshold level of R is used: here we used a threshold of R = 0.15 to ensure the reliability
261 of the orientation measurements. This threshold level has been chosen to provide the best balance
262 between a high indexing rate and a good level of data reliability.

263 For each analysis point, the Nelder-Mead optimisation method was used to refine the orientation
264 measurement as follows (43; Nelder and Mead, 1965). Small variations in the crystallographic
265 orientation, deviating from the originally measured orientation, were considered in order to create
266 new pattern templates: each of these were matched against the experimental TKD pattern and a
267 new R value was calculated. This process was repeated to maximise the R value, until successive
268 measurements generated R values differing by less than a pre-determined threshold, in this case <
269 0.0005. This orientation refinement process results in measurements with a significantly higher
270 angular precision than those measured using conventional Hough-based indexing, as described in
271 [35] Nolze et al. (2018).

272 The HAp structure belongs to the low hexagonal Laue group (6m) and, as such, lacks the basal mirror
273 plane of high hexagonal phases. However, the HAp structure is close to having high hexagonal
274 symmetry and therefore, for example, the diffraction patterns for the <0001> (+c) direction are very
275 similar to those for the <000-1> (-c) direction (referred to as pseudosymmetry). This can, for some
276 crystallite orientations, result in systematic misindexing of the TKD patterns when using the Hough
277 transform indexing method. Therefore each TKD pattern was also matched against templates for the
278 pseudosymmetry related orientation, defined by an orientation rotation of 180° about <-1-120>, in
279 order to determine the correct orientation (i.e. the solution with the highest R value). An additional
280 pseudosymmetric relationship, represented by a 90° rotation about the <-12-10> axis, was also
281 tested and corrected in the same way.

282 Many of the processes used for the generation and correlation of templates in such a dynamic way,
283 such as the orientation refinement and the testing for pseudosymmetry, have been described in
284 earlier hybrid pattern matching work, such as in [33] Winkelmann et al. (2020).

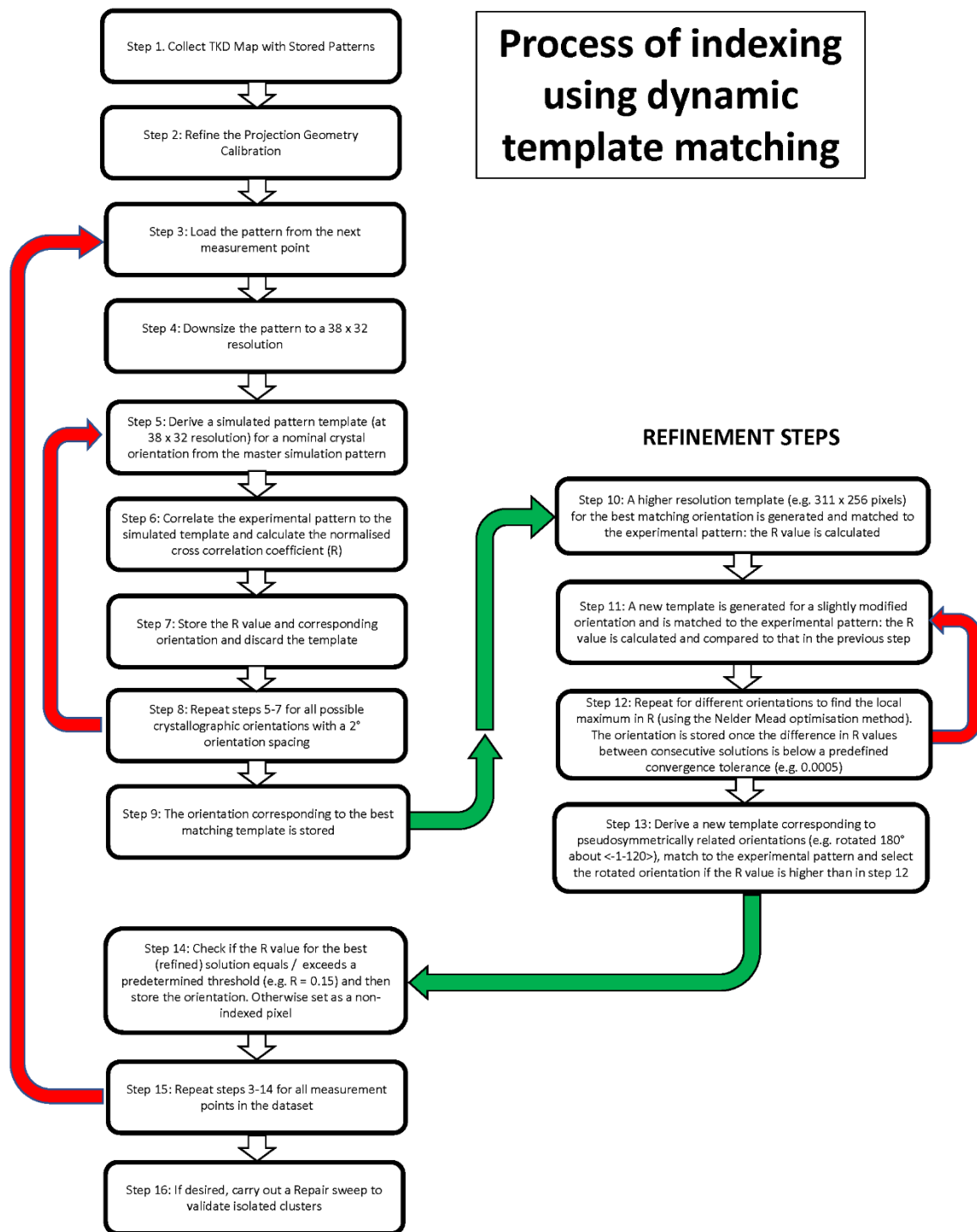
285 In order to ensure high-precision results, the pattern matching method requires a very good
286 calibration of the projection geometry for each diffraction pattern. Therefore, prior to reanalysis, the

287 calibration parameters were refined as follows, using a similar approach to that described in earlier
288 work (e.g. [33, 44]; Winkelmann et al., 2020; Friedrich et al., 2018):

- 289 1. 8 points were manually selected across the analysed area on the basis of having relatively
290 good quality diffraction patterns. Although this process can be automated, in this case the
291 generally poor diffraction pattern quality within the dataset necessitated manual point
292 selection. Points were chosen that had been successfully indexed using the Hough transform
293 indexing method.
- 294 2. As described above, for each calibration point the pattern matching process would be used
295 to refine the solution and to test against the pseudosymmetrically related solutions.
296 However, during the optimisation process, changes to the projection geometry (i.e. the
297 pattern centre position and the detector distance) would also be adjusted to find the
298 optimal values.
- 299 3. The refined calibration parameters were then used to calculate optimal calibration values
300 for each point in the TKD dataset.

301

302 Using the improved calibration parameters, the dataset was then reprocessed using a dynamic
303 template matching (DTM) approach to indexing. The step by step process of DTM indexing and
304 subsequent orientation refinement is schematically illustrated in a flow diagram, Figure 2. Following
305 the initial data collection, master pattern simulation and calibration geometry refinement (e.g. steps
306 1 – 2 in Figure 2), the following process was carried out. At each point, the experimental TKD pattern
307 was matched against simulated TKD pattern templates for the HAp phase for all possible
308 orientations: no orientation data derived from Hough-based indexing were used in this process (i.e.
309 any pre-existing indexing result was disregarded) – steps 3 - 8. The pattern templates were
310 generated using the calibration parameters at each point and with an orientation spacing of 2°. Note
311 that the templates are not stored on disk, with each one created and then the normalised cross
312 correlation coefficient between the template and the experimental Kikuchi pattern is calculated on-
313 the-fly on the GPU, and then the template is discarded. Although the dictionary indexing method can
314 also be used in a “dynamic” way (e.g. [46] Jackson et al., 2019), this involves precalculating blocks of
315 simulated templates which are then passed to a GPU for the pattern matching process. The DTM
316 approach is truly dynamic, with each simulated template only created when needed, giving the
317 technique a greater flexibility in terms of the subsequent solution refinement, as described below. A
318 template resolution of 38 x 32 pixels was used, and the experimental pattern at each point was also
319 binned down to the same pixel resolution. As in the dictionary indexing method, the simulated
320 template that produced the highest cross correlation coefficient (R) was selected as the correct
321 orientation (step 9). The initial DTM indexing method, as for dictionary indexing, produces
322 discretised orientation measurements at the initial orientation spacing, here 2°. However, the
323 dynamic nature of the method enables a subsequent orientation refinement process to be carried
324 out immediately, using the optimisation approach described previously (steps 10 – 14). Unlike the
325 initial DTM indexing, this orientation refinement was carried out at a higher pattern resolution (both
326 experimental and simulation), 321 x 256 pixels, binned down by a factor of 2 from the stored TKD
327 patterns. Once again, the patterns were also matched to simulations corresponding to the
328 pseudosymmetrically equivalent orientations to eliminate any systematic misindexing (step 13).



329

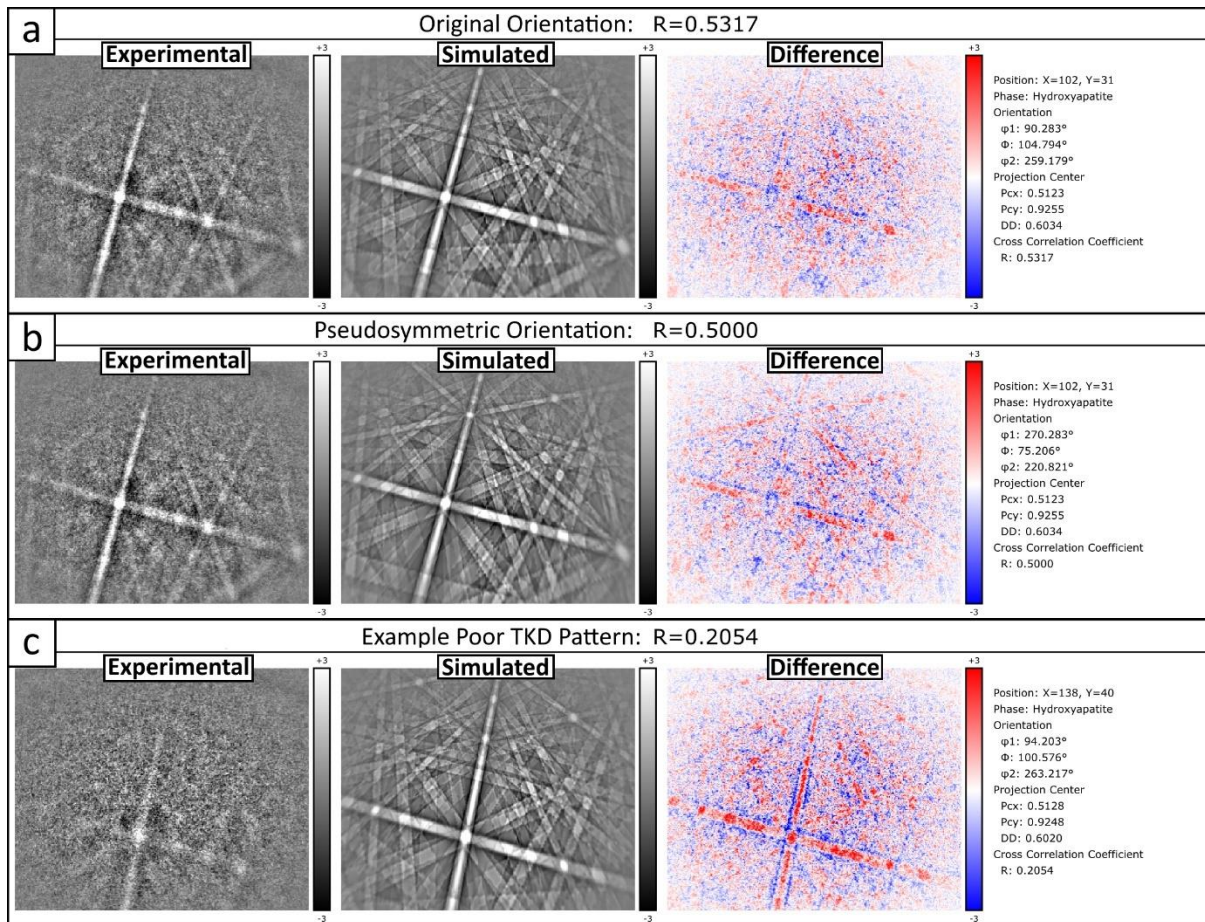
330 **Figure 2.** The step by step procedure for TKD pattern indexing using the DTM method, with
 331 subsequent orientation refinement. See text for full details.

332 The process was then repeated for all points in the dataset: due to the relatively large numbers of
 333 templates being generated at each point (typically ~200,000), the analysis speed is significantly
 334 increased by use of a graphical processing unit (GPU). In this case a low specification NVIDIA GeForce

335 GTX 1050 Ti GPU was used (4 Gb memory, 768 CUDA Cores), enabling an indexing and refinement
336 speed of ~8 patterns per second.

337 An additional method, following the DTM indexing and subsequent orientation refinement, was also
338 used to improve the indexing rate of the dataset and to remove any potentially incorrect
339 (misindexed) measurements. Although the DTM process (as with dictionary indexing) is far less likely
340 to generate incorrect solutions than the conventional Hough-based indexing method, the poor
341 quality patterns, low pattern resolution during the DTM process (38 x 32 pixels) and the 2°
342 orientation spacing between templates can all result in isolated indexing errors. This “Repair Sweep”
343 within the MapSweeper software uses the indexed orientation of neighbouring pixels as the starting
344 orientation for the template simulation. In this way isolated orientations (or small clusters of
345 orientations, with an area of 5 pixels or smaller) were checked against neighbouring measurements,
346 either validating the original indexed solution or correcting them to an orientation close to that of
347 adjacent points, based on which gave the highest R value. Likewise, the stored TKD patterns at non-
348 indexed points were compared to simulated templates generated using the orientations of
349 neighbouring, indexed points and accepted if the final refined solution had an R value exceeding the
350 0.15 threshold. This repair process was also carried out at a higher resolution than the initial DTM
351 indexing process (using a 321 x 256 pixel resolution) and so some improvements were typically made
352 to the DTM indexed data (in this case, 2015 measurements were modified, including 236 points that
353 were previously unindexed and 1779 points (~ 6% of the whole dataset) that had their orientation
354 changed). As before, the orientation measurements were refined and the final result was only
355 accepted if $R > 0.15$. This method ensures that map points with patterns which do not allow a
356 reliable indexing are assigned as zero solutions due to the correspondingly low R values, and that no
357 orientation data were interpolated from existing measurements (e.g. as derived from Hough
358 transform indexing). In each step of the DTM method, the orientation refinement and the
359 subsequent Repair Sweep, the underlying experimental pattern at each pixel is the fundamental
360 source of the derived orientation and phase solution. At no point during the DTM indexing,
361 refinement and subsequent repair process were the full 622 x 512 pixel resolution TKD patterns
362 used: this was in part because of the relatively poor quality of the HAp patterns but also because the
363 process of pixel binning within the software results in an improvement in the signal to noise ratio in
364 the patterns. The refinement and repair steps would have been slower if using the full resolution,
365 with no corresponding benefit in precision or accuracy of the final result.

366 An example of the pattern matching is provided in Figure 3. Here, in Figure 3a, a relatively high
367 quality TKD pattern from within a HAp crystallite is shown with the best fit matching template for
368 both the originally indexed orientation (from the DTM indexing process and subsequent refinement)
369 and the rotated, pseudosymmetric solution (Figure 3b). The similarities between the 2 solutions are
370 clearly visible, but the presence or absence of simulated Kikuchi bands for each solution results in a
371 significant difference between the normalised cross correlation coefficient ($R = 0.5317$ compared to
372 $R = 0.5000$), with the original orientation matching best. In Figure 3c the result for a poorer quality
373 TKD pattern is shown: with an R value of 0.2054, this still exceeds the minimum threshold for
374 acceptable pattern correlation ($R = 0.15$). Such a poor quality pattern would not be indexed using
375 conventional Hough-based indexing methods, thus demonstrating the robustness of the DTM
376 indexing process.



377

378 **Figure 3.** Example pattern matching results for good and poor quality TKD patterns from HAp
 379 crystallites. Left – experimental TKD pattern. Centre – best fitting dynamical simulation. Right –
 380 difference between experimental and simulated patterns. Scales are given in standard deviations
 381 from the mean value within each image. (a) TKD pattern 1: best fitting orientation, with a normalised
 382 cross correlation coefficient, $R = 0.5317$. (b) TKD pattern 1: the equivalent pseudosymmetric
 383 orientation, rotated 180° about $\langle -1-120 \rangle$, with $R = 0.5000$. (c) TKD pattern 2: an example of a poor
 384 quality TKD pattern, still with robust indexing, albeit with a lower R value ($R = 0.2054$).

385 Following completion of the pattern matching reanalysis, which took a total of ~ 70 minutes, the data
 386 were stored as a new dataset for further analysis within the AZtecCrystal software.

387 2.6 Data Processing

388 The enhanced data following the reanalysis using pattern matching were then processed using the
 389 data analysis tools within the AZtecCrystal software. The data were firstly cleaned using a single
 390 iteration of the “AutoClean” function: this removes isolated orientation measurements and
 391 performs a 2-pass clean up, replacing non-indexed pixels with adjacent, indexed values for pixels
 392 firstly with 6 indexed neighbours and then 5 indexed neighbours. This ensures that more complete
 393 boundary information between grains can be calculated.

394 Following cleaning, routine analyses of the data were performed in order to determine the grain size
 395 and shape, the texture (or crystallographic preferred orientation), the extent of deformation or
 396 intra-crystallite strain and to map out the key microstructural characteristics of the HAp crystallites
 397 within this enamel sample.

398

399 2.7 TEM Imaging

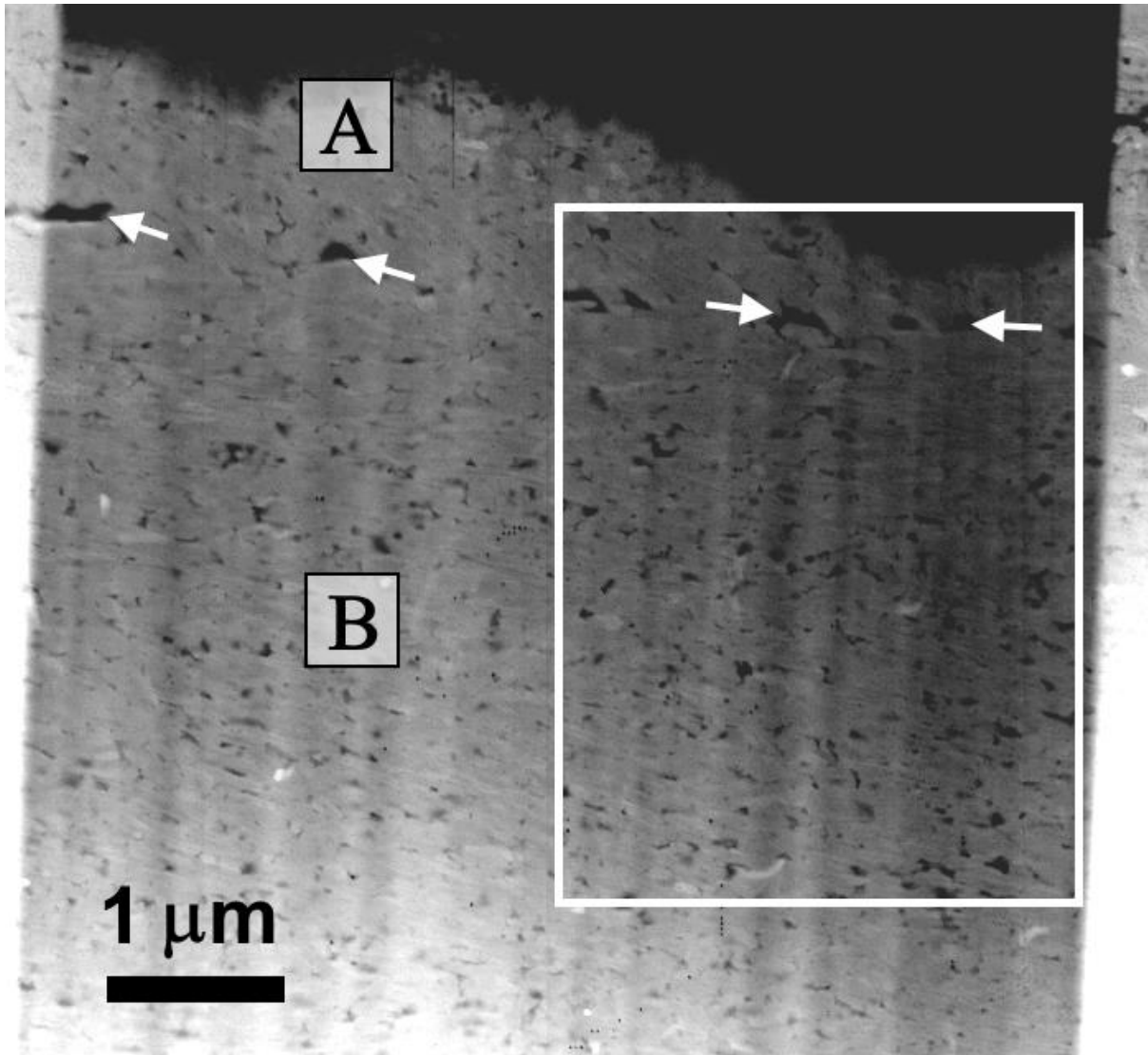
400 TEM analyses were carried out using a FEI Titan3 Themis G2 S/TEM operated at 300 kV with a Gatan
401 OneView 16 Megapixel CMOS digital camera for collecting bright-field TEM images. The TEM images
402 were collected at a screen current of 3 nA.

403 Note that the earlier TKD analyses caused noticeable damage to the TEM sample. At each point
404 analysed by TKD, a damage spot was clearly observable in the subsequent TEM images. Although the
405 damage spots enabled easy correlation between the TEM images and the TKD results, they also
406 obscured some of the HAp structures and thus most TEM imaging was performed on areas
407 immediately adjacent to the TKD analysis region. A discussion about the potential impact of the
408 beam damage during the TKD analysis is provided in the discussion section.

409

410 **3. Results**

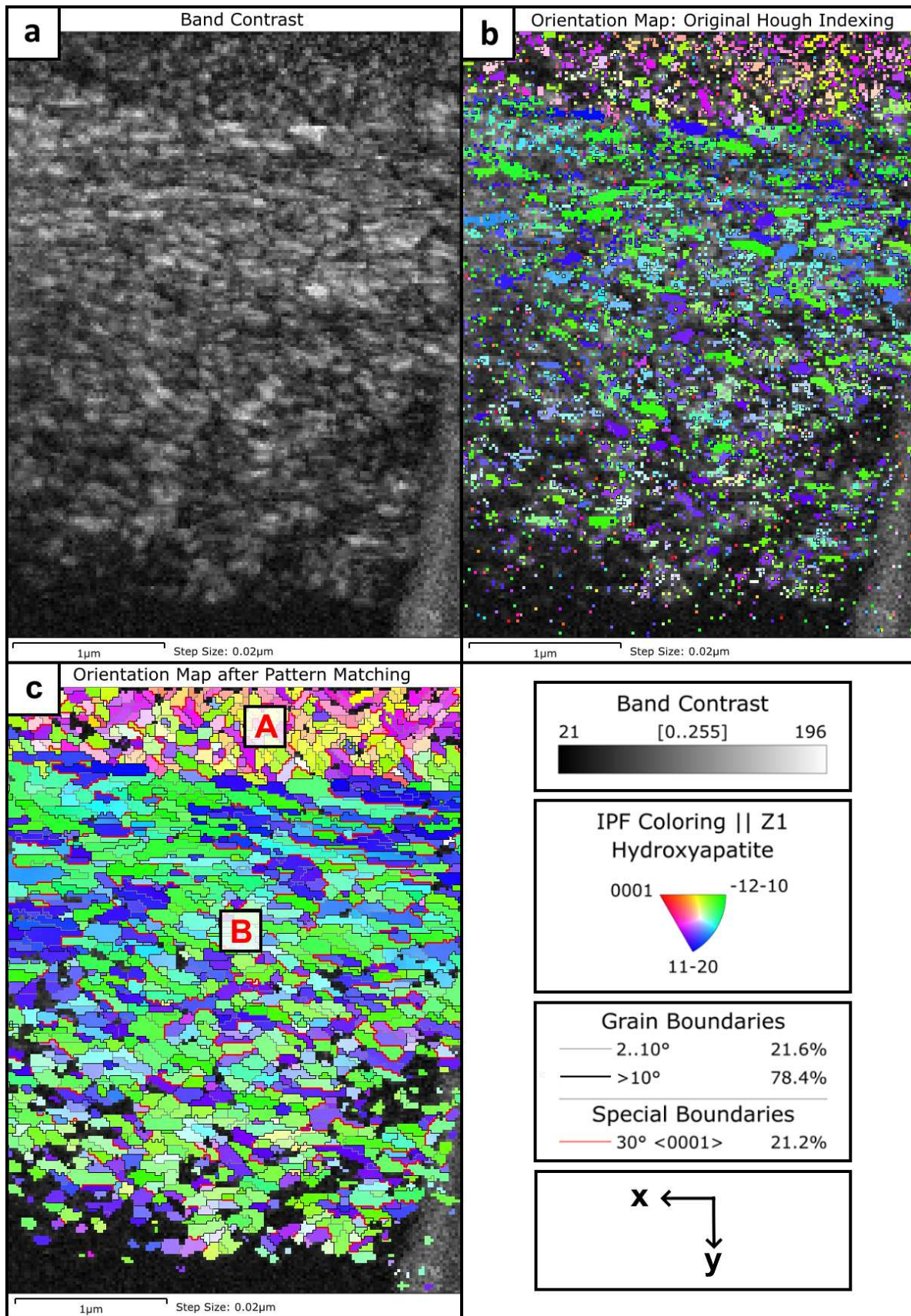
411 A forescatter detector (FSD) darkfield image of the FIB-prepared sample is shown in Figure 4. The
412 contrast has been enhanced to highlight the signal variations within the mapped area (marked by
413 the white box) – some minor thickness variations due to the FIB milling are visible as vertical
414 curtains. The image provides some indication of the HAp crystallite size and shape, with elongated
415 crystallites visibly aligned horizontally in the image, with an approximate length of a few hundred
416 nm. Towards the upper part of the area, as marked by the white arrows, a linear series of voids
417 appears to separate 2 domains with differing crystallite alignments, labelled in Figure 4 as domain A
418 and B.



419

420 **Figure 4.** A forescatter detector (FSD) darkfield image of part of the FIB-prepared sample showing the
 421 general crystallite structure within the enamel. A boundary between 2 domains differently oriented
 422 HAp crystallites is approximately marked by a series of voids, highlighted by the white arrows. The
 423 domains are labelled A and B (refer to the text for details). The white box marks the TKD analysis
 424 area. Note that the contrast has been stretched to enhance the crystallographic contrast, making the
 425 thinnest area at the top of the image appear black. The sample thickness increases towards the
 426 lower edge of the image, resulting in a stronger FSD signal.

427 The TKD mapping highlights these structural features more clearly. The band contrast map (Figure
 428 5a), a measure of the quality of the TKD pattern at each point, shows the general crystallite structure
 429 across the area and clearly emphasises the difference between the 2 domains, based on the
 430 crystallite size and shape. Towards the lower part of the area the pattern quality dropped off
 431 significantly, primarily due to an increased sample thickness in these regions coupled with some
 432 shadowing effects from the thicker margins of the FIB-prepared sample.



433

434

435

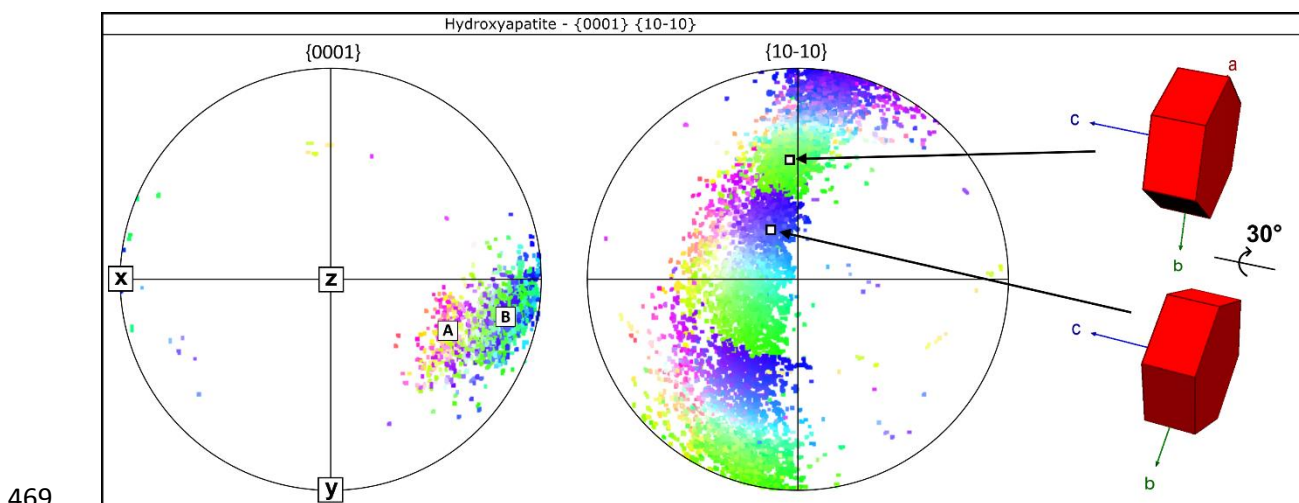
436

Figure 5. Results of TKD mapping of the enamel HAp crystallites. (a) Band contrast (diffraction pattern quality) map – lighter shades indicate higher contrast (stronger) TKD patterns. (b) Orientation map following convention Hough-transform indexing: the inverse pole figure colouring

437 *scheme shows the crystal direction parallel to the surface normal (IPF-Z) and is superimposed over*
 438 *the band contrast map – initial indexing success rate 29.1%. (c) IPF-Z orientation map following*
 439 *indexing using dynamic template matching, with only minor subsequent data cleaning (see text for*
 440 *details) – indexing success rate 71.8%, rising to 80.4% after cleaning. The two clearly distinct domains*
 441 *are labelled A and B, high angle boundaries >10° are marked in black, low angle boundaries (2-10°) in*
 442 *grey and boundaries within 10° of a 30° rotation about the <0001> axis are marked in red. The*
 443 *boundary fractions in the legend refer to (c) only. The scale bar in each image marks 1 μm.*

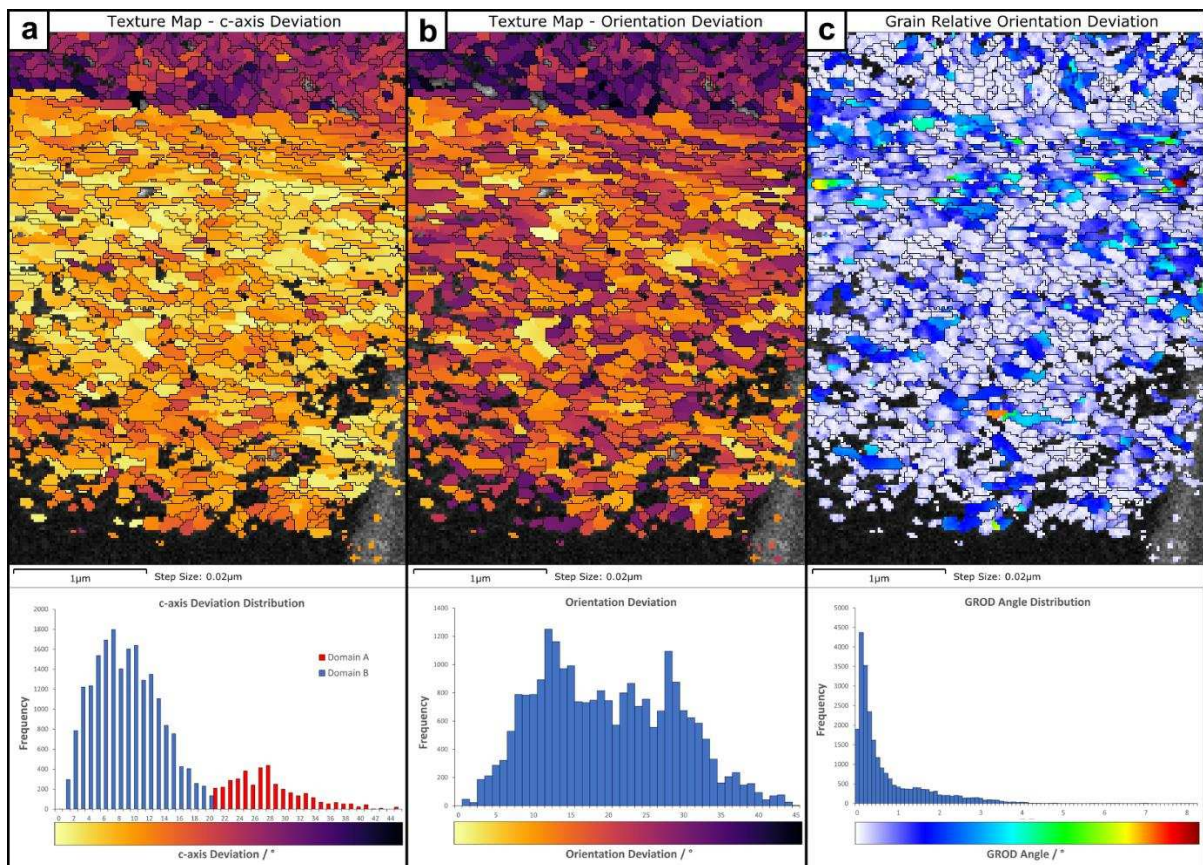
444 The initial indexing rate using the Hough transform method was only 29.1%, with the orientation
 445 map shown in Figure 5b. Although this does provide evidence of different textures in the upper and
 446 lower domains (as indicated by the different colours using the inverse pole figure colouring scheme),
 447 the low indexing rate prevents reliable analyses of the crystallites or any local variations in
 448 orientation. However, following the pattern matching reanalysis, the quality of the data is
 449 dramatically enhanced; here the indexing rate (without any further data cleaning) is 71.8% and the
 450 crystallites across most of the mapped area are effectively resolved (Figure 5c). In this map the 2
 451 aforementioned domains are clearly visible and are labelled “A” and “B”. Following the auto-clean
 452 process in AZtecCrystal, an additional 8.6% of originally unindexed pixels were assigned the
 453 orientation value of a neighbour, resulting in 80.4% of all measurement points having orientation
 454 data. This is sufficiently high to be able to measure reliably the crystallites and their orientations,
 455 boundaries within and between crystallites and to characterise the intra-crystallite deformation.

456 Figure 6 shows the texture (or crystallographic preferred orientation) of the HAP crystallites in this
 457 area represented in pole figures, plotting the poles to the {0001} and {10-10} planes; each
 458 measurement is plotted using the corresponding colour from the orientation map, Figure 5c. The
 459 {0001} pole figure shows 2 notable clusters that correspond to the domains (A and B) visible in
 460 Figure 5c. The c-axes in domain A are oriented at a significant angle to the plane of the sample, ~35°,
 461 whereas in domain B they are closer to the plane, at ~15°. The {10-10} pole figures show that, for
 462 both domains, there are 2 sub-clusters of orientations rotated 30° about <0001> from each other, as
 463 shown by the yellow and purple colours (for domain A) and the green and blue colours (for domain B)
 464 in both Figure 6 and Figure 5c. These orientations, for domain B, are illustrated by the unit cell
 465 displays in Figure 6. The boundaries corresponding to these 30° rotations about the c-axis have been
 466 coloured in red in Figure 5c: over the whole area, ~21.2% of all high angle boundaries (here defined
 467 as those with a disorientation angle > 5°) have a disorientation angle and axis within 10° of this 30°
 468 <0001> relationship.



470 **Figure 6.** Pole figures derived from the TKD measurements of HAp orientations, showing the poles to
 471 the {0001} planes (left) and poles to the {10-10} planes (right) (upper hemisphere). Each point
 472 corresponds to an individual measurement and the colour scheme is the same as used in the TKD
 473 orientation map in Figure 5c. The clusters corresponding to domains A and B are highlighted in the
 474 {0001} pole figure. Example 3D unit cell orientations (in the same reference frame as the images and
 475 TKD maps) are shown to the right, corresponding to typical orientations within domain B that are
 476 related by a 30° rotation about the c-axis.

477 The texture of the crystallites can also be visualised using texture component maps. In Figure 7a, the
 478 deviation of the c-axis orientation of each point away from the average c-axis orientation for all
 479 crystallites in domain B is plotted, up to a maximum deviation of 45°. This shows that most
 480 crystallites within domain B have their c-axes within 15° of this average orientation, whereas those
 481 in domain A are disoriented 20-35° from this orientation. However, if the full crystallographic
 482 orientation is considered, the spread of orientations is significantly greater. Figure 7b shows the full
 483 orientation deviation for each measurement away from the average orientation for crystallites in
 484 domain B, once again up to a maximum of 45°. Now the spread of orientations within domain B
 485 extends to >30°, with those points in domain A up to 45° disoriented.



486 **Figure 7.** Maps showing local and intra-crystalline orientation variations in the enamel, as measured
 487 by TKD. (a) Texture map showing the deviation in c-axis orientations (up to 45°) from the average c-
 488 axis orientation within domain B. The histogram below shows the frequency distribution of all c-axis
 489 deviations, with an x-scale from 0 – 45°, and highlights the differences between domain A (red) and
 490 domain B (blue). (b) Texture map showing the absolute orientation deviation (up to 45°) from the
 491 average orientation within domain B. The histogram below shows the frequency distribution of all
 492 orientation deviations, with an x-scale from 0 – 45°. (c) A grain relative orientation deviation (GROD)
 493 map highlighting the intracrystalline orientation within each grain / crystalline. The deviation of each
 494

495 *measurement from that grain's average orientation is plotted, up to a maximum of 8.25° and the*
 496 *frequency distribution for all measurements is shown in the histogram below. The scale bar in each*
 497 *image marks 1 μm.*

498 Within each crystallite (defined as areas bounded by boundaries with disorientations > 5°) there is
 499 also significant variation in orientation, as shown in Figure 7c. Here the average orientation of each
 500 crystallite is taken as a reference orientation, and then the disorientation between the reference and
 501 each measured orientation is plotted (sometimes referred to as a grain relative orientation deviation
 502 (GROD) map). Although most crystallites only have 1-2° of orientation deviation, many of the more
 503 elongate crystallites in the upper part of domain B have higher internal orientation deviations,
 504 frequently in the 3-6° range.

505 The crystallite size was determined using a threshold disorientation angle of 5° and a minimum size
 506 of 5 pixels, and the results are presented in Table 1. The statistics are presented for the whole
 507 dataset, as well as domains A and B individually. In total 1103 crystallites were detected, with a
 508 mean size (area-weighted equivalent circle diameter) of 129 nm. The crystallites have, on average, a
 509 high aspect ratio of 2.5, but the aspect ratio is significantly higher for domain B (2.62) than domain A
 510 (2.1). As seen in the orientation map (Figure 5c) the long axes of crystallites in domain B are oriented
 511 at a shallower angle to the map X direction than those in domain A.

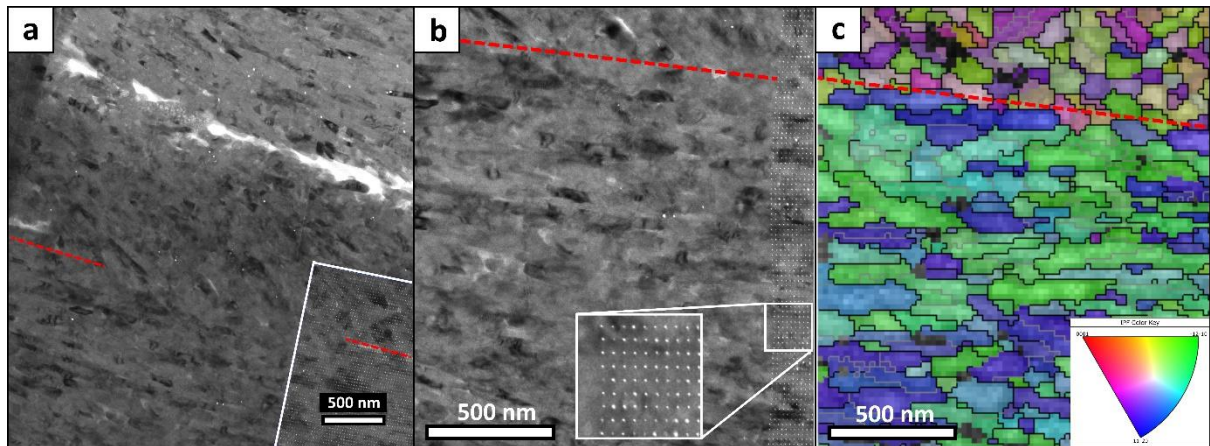
512

	Number	Mean Area Weighted Equivalent Circle Diameter (nm)	Mean Aspect Ratio	Mean Length of Major Axis (nm)	Mean Length of Minor Axis (nm)	Average Angle between Major Axis and Map X direction
Whole Dataset	1103	129 ± 1.1	2.51 ± 0.04	155 ± 2.7	64 ± 0.7	24.2°
Domain A	261	108 ± 1.7	2.1 ± 0.06	126 ± 4.1	63 ± 1.2	37.6°
Domain B	847	134 ± 1.4	2.62 ± 0.05	163 ± 3.3	65 ± 0.8	20.1°

513 **Table 1.** Table showing grain measurements (with standard errors) from the TKD dataset, with grains
 514 defined by a boundary disorientation of >5°. Grains belonging to domains A and B (as defined in
 515 Figure 5c) are measured separately. Note that some grains are counted as being in both domains A
 516 and B.

517 TEM imaging of the sample following TKD mapping highlights the dominant HAp crystallite
 518 structures, with a preferred alignment of elongated crystallites within individual domains in the TEM
 519 foil (Figure 8). The area analysed by TKD is characterised by discrete damage spots which are visible
 520 in the lower right corner of Figure 8a, and on the right edge of the higher magnification image in
 521 Figure 8b. These brightfield images show the different crystallite grain morphologies within each
 522 domain, and the boundary between the domains can be readily traced (as approximately shown by
 523 the red dashed lines in Figure 8, manually drawn based on the crystallite c-axis orientations). In the
 524 higher magnification image (Figure 8b) the crystallites appear to be 100s nm long and typically 50-
 525 100 nm wide. However, the part of the TKD orientation map shown in Figure 8c (which aligns directly
 526 with the damage spots on the right of Figure 8b) shows that the true crystallite size is significantly
 527 larger than appears in the TEM image. Most of the crystallites measured by TKD contain low angle
 528 boundaries (marked by grey lines in Figure 8c) which are typically aligned with their long axes,
 529 indicating that many of the structures visible in the TEM images are likely to be “crystallites” or

530 subgrains that are disoriented by only a few degrees from their neighbours (and would thus not be
531 classed as separate grains, separated by high angle grain boundaries).



533 **Figure 8.** (a) Brightfield TEM image of part of the enamel sample, showing the overall crystallite
534 structure. The TKD area of analysis is marked by the white box in the lower right corner and the
535 damage spots. (b) Higher magnification TEM brightfield image, rotated so as to be aligned with the
536 TKD analysis area. The white damage spots on the right of the image indicate the TKD measurement
537 locations, as shown in the higher magnification inset. (c) A part of the TKD orientation map
538 (following data cleaning) using the IPF-Z colouring scheme (inset). Black and grey lines mark high
539 angle (>10°) and low angle (2-10°) boundaries respectively. The left edge of the map area aligns with
540 the left edge of the damage spots visible in (b). In all images the scale bars mark 500 nm and the red
541 dashed lines indicate the approximate border between domains A and B.

542

543 4. Discussion

544 4.1 TKD Analysis of Biomineralised HAP

545 A full crystallographic analysis of dental enamel structures using electron diffraction in the SEM
546 requires a combination of high spatial resolution and reliable diffraction pattern indexing methods.
547 Although previous work (27-28; Koblischka-Veneva et al., 2018; 2019) has highlighted the potential
548 of the TKD method for enamel characterisation, the data provided in that work does not stand up to
549 qualitative interrogation, as explained in the introduction. There are 2 clear challenges for the
550 reliable characterisation of HAP crystallites – the extreme beam sensitivity of the HAP structure and
551 the generally poor quality of any resulting diffraction pattern. TKD has been shown to deliver the
552 required spatial resolution for effective mapping of HAP crystallites, but conventional Hough-based
553 indexing methods do not give robust results, due to the lack of sufficiently well-defined Kikuchi
554 bands in each individual TKD pattern. Most Hough-based indexing approaches require the correct
555 identification of at least 6 Kikuchi bands in each pattern in order to give robust indexing results;
556 although the higher-quality patterns in these data (as exemplified in Figure 3a) can be successfully
557 indexed via the Hough-transform method, most patterns lack the required signal to noise ratio or
558 Kikuchi band definition for reliable indexing in this way. Pattern matching methods do not suffer
559 from this drawback: the indexing is based on the pixel-to-pixel correlation between the experimental
560 pattern and a simulated pattern, so does not require well-defined Kikuchi bands for successful
561 interrogation. The increase in indexing rate over Hough-based indexing, from 29.1% to 71.8%,
562 demonstrates the efficacy of the dynamic template matching indexing method employed in this
563 study. We have demonstrated that, following further minor cleaning of the data, it is possible to

564 characterise effectively the detailed crystallite structure, the full orientation at each point and the
565 intra- and inter-crystallite boundaries within dental enamel. This has not been effectively
566 demonstrated previously and opens the door to a more thorough interrogation and understanding
567 of the HAp structures in dental enamel.

568 However, even with dynamic template matching, there are TKD patterns that could not be reliably
569 indexed: this is particularly true at the lower part of the analysis area, where the increased thickness
570 of the FIB lamella results in greater electron scattering through the sample, a corresponding increase
571 in the TKD pattern source volume and a subsequent drop in the pattern sharpness and quality (e.g.
572 Figure 4 and Figure 5a). One of the strengths of pattern matching methods is that they can provide a
573 best-fit solution for any acquired pattern, regardless of the pattern quality. However, this also can be
574 one of the weaknesses of the method – without a suitable minimum threshold for the image
575 similarity (between the experimental and simulated patterns), incorrect solutions would be obtained
576 for the poorest patterns in any dataset. Here, the acceptance of solutions that give a normalised
577 cross correlation coefficient > 0.15 minimises this risk, but for any pattern matching method the
578 setting of such a threshold remains critical for a robust microstructural characterisation. Adjusting
579 the R threshold to a higher value (e.g. $R = 0.2$) would reduce the indexing success rate, but eliminate
580 most if not all falsely indexed points; likewise a lower R threshold (e.g. $R = 0.1$) would result in a
581 higher indexing success rate but at the expense of data reliability. The selected value of $R = 0.15$
582 provides a suitable balance between the two, with almost all false solutions corrected during the
583 final stage of the pattern matching process (the “Repair Sweep”, Figure 2, Step 16).

584 4.2 The Impact of Beam Damage to HAp Crystallites during TKD Analyses

585 The spatial resolution demonstrated by the TKD data shown here, with a 20 nm measurement step
586 size, is sufficient for the characterisation of all but the very smallest HAp crystallites. However, the
587 beam sensitivity of the HAp crystallites is clear from the damage visible in the TEM images after the
588 TKD analysis (Figure 8). Each damage spot is approximately 2-3 nm across, although occasionally the
589 damage is more extensive, in the 5-10 nm diameter range. With a 20 nm step size, these damage
590 spots do not overlap (as visible in Figure 8b) and subsequently there is no progressive accumulation
591 of damage as the TKD analysis is carried out. Therefore, with these beam conditions and pattern
592 exposure times, we would expect a lower limit for the measurement step size to be in the range of
593 10-15 nm, below which damage would accumulate from point to point or row to row, reducing the
594 quality of the TKD data. For the data presented here, the electron dose at each point was 420 nAms
595 ($3.9 \text{ nA beam current} \times 108 \text{ ms exposure}$); this is a relatively high dose required in part by the weakly
596 diffracting nature of HAp, but also due to the inefficiency of the TKD geometry. Across the whole
597 mapped area, this dose equates to $\sim 6.5 \times 10^4 \text{ e}^-/\text{\AA}^2$, which is towards the upper levels of electron
598 doses in previous TEM-based studies of irradiation damage of apatite crystals (e.g. 47-48; Brès et al.,
599 1991; Meldrum et al., 1997). However, the characteristics of a TKD analysis in the SEM is significantly
600 different from TEM imaging. Standard TEM imaging exposes the whole imaged area to a uniform
601 dose, whereas in TKD mapping the beam is focused into discrete spots, the size of which is
602 dependent on the diameter of the focused electron beam (although scattering of electrons through
603 the sample thickness will result in a slight broadening of the interaction volume). For a high-
604 performance FEG-SEM, as used in this study, it is reasonable to assume that the beam diameter will
605 be approximately 2 nm: therefore the electron dose is extremely high (e.g. $\sim 8 \times 10^6 \text{ e}^-/\text{\AA}^2$) at these
606 discrete analysis spots but is negligible in the surrounding material. In this study, with a
607 measurement spacing of 20 nm, this means that $\sim 99\%$ of the surface area will have negligible direct
608 dose (these areas will be exposed to the electron beam only during initial imaging, when FSD images
609 were collected with a dwell time per pixel of 60 μs , giving a dose of $\sim 0.4 \text{ e}^-/\text{\AA}^2$).

610 A reduction of the electron dose, whilst maintaining the same quality of TKD pattern, would enable a
611 smaller measurement step size and thus a higher spatial resolution of the analyses. This could be
612 achieved by positioning the EBSD detector closer to the sample (here the detector distance, the
613 distance from the electron beam – specimen interaction point and the detector phosphor screen,
614 was 14.1 mm), using an alternative TKD geometry (e.g. on-axis TKD) or by improving the sensitivity
615 of the EBSD detector. Although pattern matching indexing methods, such as dynamic template
616 matching, do enable successful indexing of poorer quality TKD patterns (e.g. collected using a lower
617 electron dose), the reliability of the data would decrease and there would be more systematic
618 indexing errors resulting from the pseudosymmetry of the HAp structure. There is the possibility that
619 a lower electron dose would lessen the localised damage to the HAp structure and therefore
620 maintain or improve the TKD pattern quality, but in testing on these samples this was not observed.
621 Once again, the importance of setting of an appropriate pattern matching quality threshold is critical
622 for ensuring the integrity of data derived from pattern matching interrogation of biomineralised HAp
623 structures.

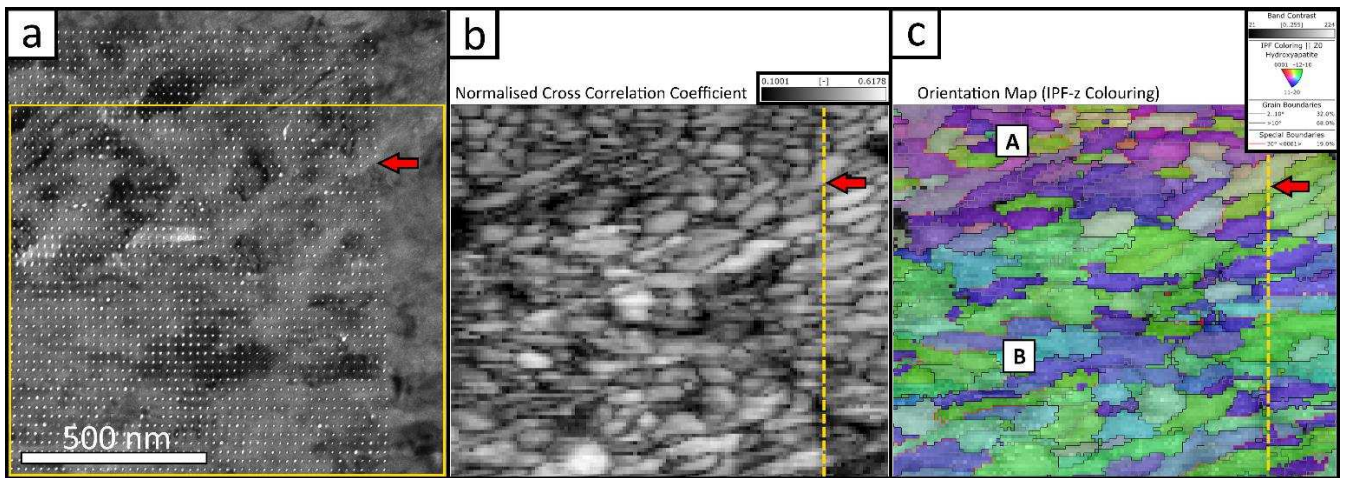
624 Based on the difference between enamel HAp crystallite sizes measured using TKD mapping in this
625 study and those reported in earlier TEM-based studies (e.g. 4; Kerebel et al., 1979), especially taking
626 into account the high electron dose used here, it must be considered whether beam damage to the
627 HAp structure is affecting the reliability of the results. It is well established from previous TEM
628 studies that damage in dental enamel HAp can occur in a number of ways, including void formation,
629 amorphisation and crystallisation of CaO or CaF₂ (e.g. 47-48; Brès et al., 1991; Meldrum et al., 1997).
630 However, as previously mentioned, the characteristics of TEM imaging and TKD analyses differ
631 significantly: it is to be expected that, at the point of each TKD analysis, significant damage will be
632 caused to the HAp structure. However, there are two key points to consider when comparing to
633 previous TEM studies. Firstly, the damage will be limited to the electron-sample interaction volume
634 and its immediate surrounds, as shown by the discrete nature of the damage spots visible in Figure
635 8b. Image analysis of the damage spots in the TEM images show that these make up ~4 % of the
636 total TKD analysis area. Secondly, the TKD pattern that is collected at each point is an integration of
637 the signal for the whole dwell time at that point; therefore, even if the HAp was being damaged
638 during this process, the initial diffraction signal would likely be strong and this would decrease
639 during the pattern acquisition time (approximately 100 ms) as the crystal structure deteriorates,
640 resulting in a progressively increased level of noise in the pattern and a corresponding drop in the
641 final cross correlation coefficient following pattern matching. However, the initial higher-intensity
642 diffracted signal would likely still dominate the final TKD pattern, ensuring robust orientation
643 measurements.

644 In order to investigate potential damage during TKD analyses in more detail, an area of the sample
645 (covering part of the original TKD map area and part that had not been previously analysed) was re-
646 mapped at a higher spatial resolution (10 nm measurement spacing) and compared to the prior TEM
647 images. Figure 9 shows the results of this subsequent analysis, although note that this was carried
648 out with the sample mounted upside down compared to the previous TKD analysis and thus it is
649 impossible to carry out a direct correlation of the mapped HAp structures. There are a number of
650 conclusions that can be drawn from this follow-on analysis:

- 651 • The damage from the initial TKD mapping is almost invisible in the subsequent map results,
652 with only a slight decrease in TKD pattern quality resulting in a barely-discernible drop in the
653 subsequent cross correlation coefficient values (Figure 9b). If a subsequent measurement
654 spot was positioned over one of the pre-existing damage spots, then it would likely result in

655 a significantly reduced TKD pattern quality and a corresponding drop in the cross correlation
 656 value.

- 657 • Within the TEM image, there are some clear boundaries and crystallites that can be traced
 658 across the border of the original TKD map area, which would indicate that there was no
 659 structural modification caused by the initial TKD mapping process. These boundaries and
 660 crystallites also appear continuous across the edge of the original TKD map area in the
 661 subsequent TKD map data, once again confirming that the original analysis has not altered
 662 the HAp grain structure (as shown by the arrowed boundary in Figure 9). It is, however, clear
 663 that the HAp structure at the nm-scale has been affected, likely by either amorphisation of
 664 the crystalline lattice or by void formation (resulting in the clear damage spots in Figure 9a),
 665 but there is no evidence for this altering the grain-scale structures on the 10s to 100s nm
 666 scale. In addition, there is no evidence for any change in crystallographic orientation across
 667 the border between the originally mapped area and the adjacent region (as shown in Figure
 668 9c), confirming that, if there was any change in orientation caused by the electron beam –
 669 HAp interaction, then it is at a level below that detectable using the TKD pattern matching
 670 technique (e.g. $< 0.1^\circ$).
- 671 • There is no apparent change in the TEM image contrast or crystallite structure within and
 672 outside the originally mapped area, with the exception of the individual damage spots. This
 673 would indicate that the majority of the structure has not been modified by the TKD mapping.
- 674 • There is no evidence of crystallisation of the cubic CaO or CaF₂ phases. In all areas of this
 675 remapped region, pattern matching results were consistent with the structure remaining as
 676 crystalline HAp.



677

678 *Figure 9. Results of a follow-on TKD analysis across the edge of the originally mapped area, using a*
 679 *smaller 10 nm step size. (a) Brightfield TEM image, showing the damage spots from the first TKD*
 680 *analysis. The yellow box marks the area of the subsequent TKD analysis. (b) Normalised cross*
 681 *correlation coefficient map of the TKD results, with the scale ranging from R = 0.1 (black) to R =*
 682 *0.6178 (white). (c) Inverse pole figure (z-direction) orientation map of the same area, with high angle*
 683 *boundaries shown in black, boundaries with 30° rotations about <0001> in red and low angle*
 684 *boundaries in grey. In both (b) and (c), the edge of the original TKD analysis area is marked by the*
 685 *yellow dashed line. The red arrows mark a boundary that is clearly visible in all the images, and the*
 686 *labels A and B in (c) mark the domains visible in the previous analyses (e.g. Figure 5). The scale bar in*
 687 *(a) marks 500 nm and all images are displayed at the same scale.*

688 These observations support the argument that, although there is localised damage, this is not
 689 affecting the reliability of the TKD orientation measurements.

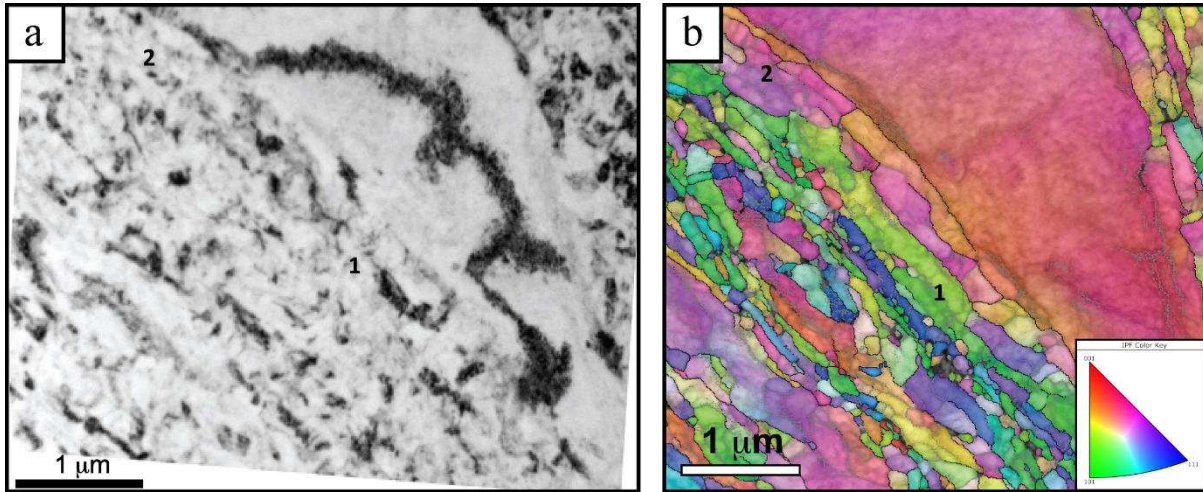
690 4.3 Comparison with TEM Imaging

691 The comparison with TEM imaging is particularly revealing, as shown in Figure 8. The morphology of
692 crystallites is very clear in the TEM images, allowing a simple identification of the 2 domains based
693 on the orientation of the crystallite long-axes (e.g. Figure 8a). However, the direct comparison
694 between the TKD orientation map (Figure 8c) and the TEM brightfield image of the immediately
695 adjacent area (Figure 8b) shows that the crystallite size, as determined from the TEM image, appears
696 much smaller than in the TKD map. Although there was minor drift during the TKD analysis, this
697 amounted to only 5.7 % in the y-direction and cannot explain the crystallite size discrepancy
698 between TKD and TEM. A closer inspection of the TKD map shows that there are multiple low angle
699 boundaries (grey lines in Figure 8c, representing crystallographic disorientations of 2-10°) and that
700 these delineate areas of a similar scale to those visible in the TEM images (i.e. 40-80 nm width, 100s
701 nm length). This is also visible in the absolute orientation deviation texture map (Figure 7b) in which
702 the subtle, low-angle orientation changes between adjacent crystallites are apparent. The same
703 observations are apparent in the follow-on TKD results, shown in Figure 9, although here the
704 normalised cross correlation map does suggest a crystallite size closer to that inferred from the TEM
705 image and reported in other TEM-based studies (e.g. 49, DeRocher et al., 2020). These observations
706 indicate that many of the crystallites in the TEM image have a crystallographic orientation very close
707 ($< 10^\circ$) to that of their neighbours. In addition, the GROD map (Figure 7c) highlights that many of the
708 crystallites also contain significant lattice distortion on the sub-100 nm scale. Although most
709 crystallites have minimal variation in crystallographic orientation ($< 1^\circ$, as indicated by dominantly
710 white shades in Figure 7c), there are many cases where the distortion extends into the 2-4° range:
711 the crystallites, as viewed in the TEM images are essentially “sub-grains” with a significant amount of
712 intra-crystallite distortion. The subdivision of larger, perfect crystallites into smaller domains with
713 slight variations in crystallographic orientation has been referred to as “crystal splitting” (e.g. 50;
714 Deng et al., 2022). Similar structures have been commonly observed in many biomineralised
715 materials, including in the calcite (CaCO_3) shells of oysters as revealed by 3D X-ray Bragg
716 ptychography (51; Mastropietro et al., 2017), and may be interpreted as a strengthening mechanism
717 or as a direct consequence of the biomineralisation process.

718 The difference in grain size between that measured using TKD orientation measurements and that
719 inferred from TEM images is not unique to HAp or to biomineralised samples. In many highly
720 deformed materials, including metals and minerals, the inferred grain size from TEM imaging is
721 consistently smaller than that measured using TKD. This is demonstrated in Figure 10, which shows a
722 brightfield TEM image and a TKD orientation map from the same area in a highly-deformed Al-Mg-Cu
723 alloy (processed with 4 passes of equal channel angular pressing (ECAP) performed at room
724 temperature). The TEM brightfield image of the matrix region (Figure 10a) can be interpreted as
725 showing a nanocrystalline grain structure, yet the TKD orientation map (Figure 10b) shows that
726 many grains are 1-5 μm long and made up of multiple, smaller domains with low angle
727 disorientations ($< 5^\circ$) between them, as marked by grains 1 and 2 in both images. These slight
728 changes in crystallographic orientation can produce significant changes in the TEM image signal but
729 should not be interpreted as representing different grains. In the same way with the HAp dental
730 enamel structures, the TEM images suggest a very small crystallite size, in the order of a few 10s nm,
731 yet many adjacent crystallites share very similar crystallographic orientations and, when measured
732 using TKD, the true grain sizes (as defined as areas bound by higher angle boundaries, $> 5^\circ$) are
733 significantly larger (Table 1). Such differences can be attributed to the quantitative nature of TKD
734 orientation maps, as well as the difference in information source volumes for the 2 techniques. It has
735 been well documented that the TKD pattern is dominantly derived from the lower (exit) surface of
736 the sample, enabling the resolution of crystallites that are significantly smaller than the sample

737 thickness (e.g. 22-23; Keller and Geiss, 2012; Trimby, 2012). This is in contrast to TEM imaging where
738 the signal is derived from the full sample thickness.

739 These factors explain the apparent discrepancy between the results presented in this work and TEM-
740 image based results from previous studies of dental enamel.



741

742 *Figure 10. Comparison between TEM brightfield imaging and TKD orientation mapping of a room*
743 *temperature deformed aluminium alloy. (a) Brightfield TEM image collected at 200 kV, showing a*
744 *large deformed grain within what appears to be a nanocrystalline matrix. (b) TKD orientation map of*
745 *the same area (collected with an 8 nm measurement spacing) showing that the matrix is mostly*
746 *comprised of long, elongate grains with significant substructure. Black lines indicate boundaries > 10°*
747 *disorientation, grey lines boundaries between 2° and 10° disorientation, colours use the inverse pole*
748 *figure colour scheme for the sample normal direction (inset). Scale bars in both images mark 1 μm,*
749 *with “1” and “2” marking the same elongate grains in both images. See text for discussion.*

750

751 4.4 New Insights into Enamel HAp Structure using Complete Orientation Measurements

752 The TKD results presented here have a significant advantage over other widely-used methods for
753 characterising HAp crystallites in dental enamel, namely the measurement of the full 3-dimensional
754 crystallographic orientation. This enables a more rigorous examination of the true crystallite size, the
755 relationship between crystallite morphology and crystallographic orientation and the absolute local
756 orientation variations.

757 The fact that the TKD measurements determine not just the c-axis orientation of the HAp crystal
758 lattice (as is common with many alternative techniques), but the full crystallographic orientation,
759 reveals a number of important observations about the enamel microstructure. Firstly, the extent of
760 orientation variation from crystallite to crystallite is significantly greater than would be measured by
761 c-axis orientations alone, as shown by the comparison between Figures 7 (a) and (b). Relative to the
762 average orientation in Domain B, the c-axes within this domain vary in orientation by up to ~15°, but
763 the full crystallographic orientation varies by up to ~30° - this increased level of orientation variation
764 will have a significant impact on the expected physical properties of the enamel. Additionally, the full
765 crystallographic orientation data highlights the systematic rotation between adjacent crystallites of
766 30° about the <0001> axis, as shown in Figures 5c and 6. These special boundaries, which would not
767 be visible if only the c-axis orientations were measured, may represent a type of twin boundary. It is
768 well understood from the study of metals and geological minerals that twins can form either as

769 growth twins or in response to deformation, and both growth twinning in biogenic aragonite and
770 deformation twinning in biogenic calcite have been widely reported (e.g. 52-54; Mukai et al., 2010;
771 Pokroy et al., 2007; Côté et al., 2015). Twinning in enamel HAp has also been widely reported, but
772 these previously-identified twin boundaries typically form straight features aligned with the long axis
773 of the HAp crystallites (i.e. parallel to the c-axis direction) (55-56; Rachinger et al., 1982; Brès et al.,
774 1986). In the TKD data presented here, the boundaries with the aforementioned 30° about <0001>
775 rotation form irregular interfaces between adjacent clusters of slightly-disoriented crystallites (red
776 boundaries in Figure 5c). This morphology is not characteristic of most twinned structures, either
777 caused by growth or deformation, suggesting that these may not be true twin boundaries but are,
778 perhaps, indicative of a systematic switch in crystallite orientation during biomineralisation that may
779 benefit the bulk physical properties.

780 There have been many studies that have inferred that the hierarchical structures visible in
781 biomineralised HAp in dental enamel result in the exceptional physical properties of the enamel
782 layer (57-58, 13; Koenigswald et al., 1992; Wegst et al., 2014; Stifler et al., 2021). The misorientation
783 between adjacent HAp crystallites has been correlated with improved crack-deflection, although
784 once again previous studies have only focused on the variation of c-axis orientations (e.g. 13; Stifler
785 et al. 2021). The results shown here highlight the importance of measuring the full crystallographic
786 orientation, as previous work neglects the role of any misorientations that involve a component of
787 rotation about the HAp c-axes. These include the anomalously abundant boundaries with rotations
788 close to 30° about <0001>, but also the smaller disorientations within and between crystallites that
789 are highlighted in Figures 7 (b) and (c). An accurate measurement of the full, true degree of crystal
790 lattice orientation variation is necessary to understand the true importance of the hierarchical
791 structures and their role in determining the enamel's physical properties.

792 4.5 Future Work

793 The method and results presented here represent a proof of concept of the potential of TKD
794 analyses, in combination with novel pattern matching methods, for the effective characterisation of
795 HAp nanostructures in biomineralised materials such as dental enamel. The high spatial resolution
796 coupled with the measurement of the full crystallographic orientation makes this a unique and
797 powerful approach, without necessitating time on expensive beamlines. It is not possible to make
798 justified statements on the detailed hierarchical structures visible in this dental enamel sample, or
799 even to interpret the nature of the domain boundary visible in these results (e.g. whether this is the
800 boundary between an adjacent prism tail and head) – for this, further analyses of multiple, larger
801 areas of TEM samples will be necessary. This will be the focus of future work on similar dental
802 enamel samples, with a correlation to the larger scale hierarchical structures and to the resulting
803 mechanical properties. As a potential avenue for future research, the analysis of the cross-sectional
804 plane of prisms, rather than their long axes, could prove to be a valuable approach for investigating
805 the structure and properties of dental enamel. By examining the cross-sectional plane, it may be
806 possible to gain a deeper understanding of the orientation and distribution of the HAp crystallites
807 within the whole prism cross-section, as well as their potential role in the mechanical properties of
808 enamel.

809

810 5. Conclusions

811 We present the first effective characterisation of HAp microstructures in human dental enamel using
812 the SEM-based TKD technique coupled with newly-developed pattern matching methods, including

813 dynamic template matching and subsequent orientation refinement. This approach delivers high
814 spatial resolution measurement of the absolute crystallographic orientation of the HAp crystallites,
815 with a significantly improved data quality compared to conventional Hough-transform based
816 indexing methods. Although localised damage to the HAp crystal structure has occurred during the
817 TKD analysis, we have shown that this has not affected the veracity of the TKD results. The TKD
818 orientation measurements have been subsequently compared to TEM images of the same and
819 adjacent areas, revealing some key differences between the results from both techniques.

820 The results highlight a number of interesting features of the HAp microstructure within the studied
821 enamel sample:

- 822 1. Many of the crystallites, as detected in the TEM brightfield images, are only slightly
823 disoriented (e.g. $<10^\circ$) from adjacent crystallites. The true grain size within the enamel layer
824 (as determined by high angle grain boundaries) is thus significantly greater than would be
825 deduced from the TEM images alone.
- 826 2. Many of the individual crystallites have significant localised orientation variation, commonly
827 with lattice rotations up to $\sim 4^\circ$.
- 828 3. Within individual domains in the enamel, there is a strong clustering of c-axis orientations
829 (up to $\sim 15^\circ$ deviation from the average c-axis orientation within each domain), but a greater
830 deviation of the full crystallographic orientation (up to $\sim 30^\circ$).
- 831 4. Many boundaries between adjacent crystallites have a rotation angle and rotation axis close
832 to 30° about the $\langle 0001 \rangle$ axis. These boundaries are commonly irregular in morphology so
833 may not be true twin boundaries.

834 The capability of the TKD method, in conjunction with pattern matching reanalysis, to determine the
835 full crystallographic orientation of the HAp crystal lattice, and not just the c-axis orientation (as with
836 many other analysis methods) enables a far more rigorous examination of the crystallographic
837 characteristics of the enamel microstructure. This additional information will help us to understand
838 better the relationship between enamel's remarkable physical properties and the crystal structure of
839 the HAp on the nanoscale, using tools widely available to many researchers. We expect to further
840 refine this method and to apply it to a wider range of enamel samples in order to characterise better
841 the relationship between the HAp nanostructures and the known structural domains within human
842 dental enamel.

843

844 **Acknowledgements**

845 Junhai Xia is thanked for providing the deformed Al-alloy sample and for collecting the TEM image
846 shown in figure 10. The data shown in figure 10 were collected at Sydney Microscopy and
847 Microanalysis, the University of Sydney, Australia. Klaus Mehnert is thanked for his help in
848 developing the pattern matching tools used in this work. The two reviewers are thanked for their
849 careful assessment of the manuscript and for constructive criticism that has led to a marked
850 improvement in this work.

851

852 **Funding**

853 This research did not receive any specific grant from funding agencies in the public, commercial, or
854 not-for-profit sectors.

856 **References**

857

- 858 1. Robinson, C., et al., The chemistry of enamel caries. *Critical Reviews in Oral Biology & Medicine*,
859 2000. 11(4): p. 481-495.
- 860 2. Robinson, C., et al., The chemistry of enamel development. *International Journal of*
861 *Developmental Biology*, 1995. 39(1): p. 145-152.
- 862 3. Elliott, J.C., Structure, crystal chemistry and density of enamel apatites, in *Dental Enamel* (Ciba
863 Foundation Symposium). 1997, John Wiley & Sons Ltd., West Sussex, UK. p. 54-72.
- 864 4. Kerebel, B., G. Daculsi, and L. Kerebel, Ultrastructural studies of enamel crystallites. *Journal of*
865 *dental research*, 1979. 58(2 suppl): p. 844-851.
- 866 5. Simmer, J.P., et al., A post-classical theory of enamel biomineralization...and why we need one.
867 *International journal of oral science*, 2012. 4(3): p. 129-134.
- 868 6. Shore, R.C., et al., Structure of mature enamel, in *Dental Enamel: Formation to Destruction* (Edited
869 by Robinson C., Kirkham J. and Shore R.C.). 1995, CRC Press, New York, USA. p. 151-166.
- 870 7. Boyde, A., The structure and development of mammalian enamel, in *Department of Anatomy*.
871 1964, University of London, London, UK.
- 872 8.. Lawn, B.R., J.J.-W. Lee, and H. Chai, Teeth: among nature's most durable biocomposites. *Annual*
873 *Review of Materials Research*, 2010. 40: p. 55-75.
- 874 9. Shore, R.C., et al., Structure of developing enamel, in *Dental Enamel: Formation to Destruction*
875 (Edited by Robinson C., Kirkham J. and Shore R.C.). 1995, CRC Press, New York, USA. p. 135-150.
- 876 10. Robinson, C., et al., Chemistry of mature enamel, in *Dental Enamel: Formation to Destruction*
877 (Edited by Robinson C., Kirkham J. and Shore R.C.). 1995, CRC Press, New York, USA. p. 167-191.
- 878 11. Poole, D. and A. Brooks, The arrangement of crystallites in enamel prisms. *Archives of oral*
879 *biology*, 1961. 5(1): p. 14-26.
- 880 12. Beniash, E., et al., The hidden structure of human enamel. *Nature communications*, 2019. 10(1):
881 p. 4383.
- 882 13. C.A. Stifler, J.E. Jakes, J.D. North, D.R. Green, J.C. Weaver, P.U.P.A. Gilbert, Crystal misorientation
883 correlates with hardness in tooth enamels, *Acta Biomaterialia*, 120, 2021, Pages 124-134, ISSN 1742-
884 7061, <https://doi.org/10.1016/j.actbio.2020.07.037>.
- 885 14. Free, R., et al., A method for mapping submicron-scale crystallographic order/disorder applied to
886 human tooth enamel. *Powder diffraction*, 2020. 35(2): p. 117-123.
- 887 15. Free, R., et al., Mesoscale structural gradients in human tooth enamel. *Proceedings of the*
888 *National Academy of Sciences*, 2022. 119(52): p. e2211285119.
- 889 16. Zaefferer, S. (2011), A critical review of orientation microscopy in SEM and TEM. *Cryst. Res.*
890 *Technol.*, 46: 607-628. <https://doi.org/10.1002/crat.201100125>
- 891 17. Borrajo-Pelaez, R. & Hedström, P. (2018). Recent Developments of Crystallographic Analysis
892 Methods in the Scanning Electron Microscope for Applications in Metallurgy, *Critical Reviews in Solid*
893 *State and Materials Sciences*, 43:6, 455-474, DOI: 10.1080/10408436.2017.1370576

- 894 18. A. Tripathi and S. Zaefferer, On the resolution of EBSD across atomic density and accelerating
895 voltage with a particular focus on the light metal magnesium. *Ultramicroscopy* 207 (2019) 112828
- 896 19. A. Pérez-Huerta, M. Cusack and C.A. Mendez (2012), Preliminary assessment of the use of
897 electron backscatter diffraction (EBSD) in conodonts. *Lethaia*, 45, 253-258.
- 898 20. A. Atakul-Özdemir, X. Warren, P.G. Martin, M. Guizar-Sicairos, M. Holler, F. Marone, C. Martínez-
899 Pérez and P.C.J. Donoghue (2021). X-ray nanotomography and electron backscatter diffraction
900 demonstrate the crystalline, heterogeneous and impermeable nature of conodont white matter. *R.*
901 *Soc. open sci.* 8202013202013
- 902 21. McGregor, M., Erickson, T.M., Spray, J.G. et al. High-resolution EBSD and SIMS U–Pb
903 geochronology of zircon, titanite, and apatite: insights from the Lac La Moinerie impact structure,
904 Canada. *Contrib Mineral Petrol* 176, 76 (2021). <https://doi.org/10.1007/s00410-021-01828-y>
- 905 22. Keller, R.R. and Geiss, R.H. (2012), Transmission EBSD from 10 nm domains in a scanning electron
906 microscope. *Journal of Microscopy*, 245: 245-251. [https://doi.org/10.1111/j.1365-](https://doi.org/10.1111/j.1365-2818.2011.03566.x)
907 [2818.2011.03566.x](https://doi.org/10.1111/j.1365-2818.2011.03566.x)
- 908 23. P. W. Trimby, Orientation mapping of nanostructured materials using transmission Kikuchi
909 diffraction in the scanning electron microscope. *Ultramicroscopy*, 120, 2012, p 16-24, ISSN 0304-
910 3991, <https://doi.org/10.1016/j.ultramic.2012.06.004>.
- 911 24. J.J. Funderberger, E. Bouzy, D. Goran, J. Guyon, H. Yuan, A. Morawiec, Orientation mapping by
912 transmission-SEM with an on-axis detector, *Ultramicroscopy*, 161, 2016, p 17-22, ISSN 0304-3991,
913 <https://doi.org/10.1016/j.ultramic.2015.11.002>.
- 914 25. G.C. Sneddon, P.W. Trimby, J.M. Cairney, Transmission Kikuchi diffraction in a scanning electron
915 microscope: A review, *Materials Science and Engineering: R: Reports*, 110, 2016, p 1-12, ISSN 0927-
916 796X, <https://doi.org/10.1016/j.mser.2016.10.001>.
- 917 26. Shen Y, Xu J, Zhang Y, Wang Y, Zhang J, Yu B, Zeng Y, Miao H. Spatial Resolutions of On-Axis and
918 Off-Axis Transmission Kikuchi Diffraction Methods. *Applied Sciences*. 2019; 9(21):4478.
919 <https://doi.org/10.3390/app9214478>
- 920 27. Koblischka-Veneva, A., Koblischka, M.R., Schmauch, J. and Hannig, M., Human dental enamel: A
921 natural nanotechnology masterpiece investigated by TEM and t-EBSD. *Nano Res.* 11, 3911–3921
922 (2018). <https://doi.org/10.1007/s12274-018-1968-1>
- 923 28. Koblischka-Veneva, A., Koblischka, M.R., Schmauch, J. and Hannig, M., Comparison of human and
924 bovine dental enamel by TEM and t-EBSD investigations. *IOP Conf. Ser.: Mater. Sci. Eng.* 625 (2019)
925 012006. DOI 10.1088/1757-899X/625/1/012006
- 926 29. Winkelmann, A. , Trager-Cowan, C., Sweeney, F., Day, A. P. , Parbrook, P. Many-beam dynamical
927 simulation of electron backscatter diffraction patterns (2007) *Ultramicroscopy* , 107, p. 414-21 DOI:
928 10.1016/j.ultramic.2006.10.006
- 929 30. Winkelmann, A. (2009), Dynamical simulation of electron backscatter diffraction patterns, in
930 *Electron Backscatter Diffraction in Materials Science* (ed. by A.J. Schwartz, M. Kumar, B.L. Adams &
931 D.P. Field), chap. 2. Springer, Berlin.
- 932 31. Chen, Y., Park, S., Wei, D., Newstadt, G., Jackson, M., Simmons, J., De Graef, M. and Hero, A.
933 (2015). A Dictionary Approach to Electron Backscatter Diffraction Indexing. *Microscopy and*
934 *Microanalysis*, 21(3), 739-752. doi:10.1017/S1431927615000756

- 935 32. Singh, S., Guo, Y., Winiarski, B., Burnett, T.L, Withers, P.J. and De Graef, M., High resolution low
936 kV EBSD of heavily deformed and nanocrystalline Aluminium by dictionary-based indexing. Sci Rep 8,
937 10991 (2018). <https://doi.org/10.1038/s41598-018-29315-8>
- 938 33. Winkelmann, A., Jablon, B.M., Tong, V.S., Trager-Cowan, C. and Mingard, K.P. (2020), Improving
939 EBSD precision by orientation refinement with full pattern matching. Journal of Microscopy, 277: 79-
940 92. <https://doi.org/10.1111/jmi.12870>
- 941 34. A. Winkelmann and G. Nolze, Chirality determination of quartz crystals using Electron
942 Backscatter Diffraction, Ultramicroscopy, 149, 2015, p 58-63, ISSN 0304-3991,
943 <https://doi.org/10.1016/j.ultramic.2014.11.013>.
- 944 35. G. Nolze, M. Jürgens, J. Olbricht and A. Winkelmann, Improving the precision of orientation
945 measurements from technical materials via EBSD pattern matching, Acta Materialia, vol. 159, pp.
946 408-415, (2018).
- 947 36. Nolze, G., Hielscher, R. and Winkelmann, A. (2017), Electron backscatter diffraction beyond the
948 mainstream. Crystal Research and Technology, 52: 1600252.
949 <https://doi.org/10.1002/crat.201600252>
- 950 37. Xu, N., et al., Nano-scale coating wear measurement by introducing Raman-sensing underlayer.
951 Journal of Materials Science & Technology, 2022. 96: p. 285-294.
- 952 38. Ishitani, T., et al., Improvements in performance of focused ion beam cross-sectioning: aspects of
953 ion-sample interaction. Microscopy, 2004. 53(5): p. 443-449
- 954 39. Oxford Instruments *.h5oia data format specification:
955 <https://github.com/oianoanalysis/h5oia> - website accessed on 25/05/2023
- 956 40. Crystallography Open Database: <http://www.crystallography.net/cod/index.php> - website
957 accessed on 25/05/2023
- 958 41. Ivanova, O.V. Frank-Kamenetskaya, A.B. Kol'tsov, V.L. Ugol'kov, Crystal Structure of Calcium-
959 Deficient Carbonated Hydroxyapatite. Thermal Decomposition., Journal of Solid State Chemistry,
960 160, 2001, p 340-349, ISSN 0022-4596, <https://doi.org/10.1006/jssc.2000.9238>.
- 961 42. Wilson, R.M., Elliott, J.C. and Dowker, S.E.P., Rietveld refinement of the crystallographic structure
962 of human dental enamel apatites. American Mineralogist, 1999, 84, p. 1406–1414.
- 963 43. Goshtasby, A.A. (2012). Similarity and Dissimilarity Measures. In: Image Registration. Advances in
964 Computer Vision and Pattern Recognition. Springer, London. [https://doi.org/10.1007/978-1-4471-
965 2458-0_2](https://doi.org/10.1007/978-1-4471-2458-0_2)
- 966 44. J. A. Nelder and R. Mead, A Simplex Method for Function Minimization, The Computer Journal, 7,
967 1965, p 308–313, <https://doi.org/10.1093/comjnl/7.4.308>
- 968 45. T. Friedrich, A. Bochmann, J. Dinger and S. Teichert, Application of the pattern matching
969 approach for EBSD calibration and orientation mapping, Ultramicroscopy, vol. 184, pp. 44-51, 2018.
- 970 46. Jackson, M.A., Pascal, E. and de Graef, M., Dictionary Indexing of Electron Back-Scatter
971 Diffraction Patterns: a Hands-On Tutorial. Integrating Materials and Manufacturing Innovation
972 (2019) 8:226–246. <https://doi.org/10.1007/s40192-019-00137-4>

- 973 47. Brès E.F., Hutchison, J.L., Senger, B., Voegel, J.-C. and Frank, R.M., HREM study of irradiation
974 damage in human dental enamel crystals. *Ultramicroscopy* 35 (1991), p. 305-322
- 975 48. Meldrum, A., Wang, L.M. and Ewing, R.C., Electron irradiation-induced phase segregation in
976 crystalline and amorphous apatite: A TEM study. *American Mineralogist* 82 (1997), p. 858-869.
- 977 49. DeRoche, K.A., Smeets, P.J.M., Goodge, B.H. et al., Chemical gradients in human enamel
978 crystallites. *Nature* 583, 66–71 (2020). <https://doi.org/10.1038/s41586-020-2433-3>
- 979 50. Deng, Z., Jia, Z., Li, L., Biomaterialized Materials as Model Systems for Structural Composites:
980 Intracrystalline Structural Features and Their Strengthening and Toughening Mechanisms. *Adv. Sci.*
981 2022, 9, 2103524. <https://doi.org/10.1002/advs.202103524>
- 982 51. Mastropietro, F., Godard, P., Burghammer, M. et al. Revealing crystalline domains in a mollusc
983 shell single-crystalline prism. *Nature Mater* 16, 946–952 (2017). <https://doi.org/10.1038/nmat4937>
- 984 52. H. Mukai, K. Saruwatari, H. Nagasawa, T. Kogure, Aragonite twinning in gastropod nacre, *Journal*
985 *of Crystal Growth*, 312, 2010, p 3014-3019, ISSN 0022-0248,
986 <https://doi.org/10.1016/j.jcrysgro.2010.07.002>.
- 987 53. B. Pokroy, M. Kapon, F. Marin and E. Zolotoyabko (2007). Protein-induced, previously
988 unidentified twin form of calcite. *PNAS (Applied Physical Sciences)*, 104 (18) 7337-7341,
989 <https://doi.org/10.1073/pnas.0608584104>
- 990 54. A. S. Côté, R. Darkins and D. M. Duffy. Deformation twinning and the role of amino acids and
991 magnesium in calcite hardness from molecular simulation, *Phys. Chem. Chem. Phys.*, 2015,17,
992 20178-20184
- 993 55. Rachinger, W.A., Phakey, P.P., Palamara, J. et al. Planar faults in dental hydroxy-apatite. *Calcif*
994 *Tissue Int* 34, 209–210 (1982). <https://doi.org/10.1007/BF02411235>
- 995 56. Brès EF, Waddington WG, Voegel JC, Barry JC, Frank RM. Theoretical detection of a dark contrast
996 line in twinned apatite bicrystals and its possible correlation with the chemical properties of human
997 dentin and enamel crystals. *Biophys J.* 1986 Dec;50(6):1185-93. doi: 10.1016/S0006-3495(86)83561-
998 5. PMID: 3801577; PMCID: PMC1329791
- 999 57. Koenigswald, W. V. and Clemens, W. A. (1992) Levels of Complexity in the Microstructure of
1000 Mammalian Enamel and Their Application in Studies of Systematics, *Scanning Microscopy: Vol. 6 :*
1001 *No. 1 , Article 16.* Available at: <https://digitalcommons.usu.edu/microscopy/vol6/iss1/16>
- 1002 58. Wegst, U., Bai, H., Saiz, E., Tomsia A.P. and Ritchie, R.O., Bioinspired structural materials. *Nature*
1003 *Materials* 14, 23–36 (2015). <https://doi.org/10.1038/nmat4089>